RAS Techniques and Instruments

RASTI **5,** 1–34 (2026) https://doi.org/10.1093/rasti/rzag069

Any colour you like: the diverse chromaticities of white dwarfs

Mark A. Hollands [1]★ Boris T. Gänsicke [1] Pier-Emmanuel Tremblay [1] and Detlev Koester [2]

[1]*Department of Physics, University of Warwick, Coventry CV4 7AL, UK*
[2]*Institut für Theoretische Physik und Astrophysik, University of Kiel, 24098 Kiel, Germany*

Accepted 2026 September 3. in original form 2026 August 11

ABSTRACT

Main-sequence stars have perceived colours ranging from orange to white to blue with increasing effective temperature. This is because their atmospheric opacities cause only minor deviations from blackbody colours when integrated over the broad-band sensitivity curves of the human visual system. White dwarfs can have much denser atmospheres, reaching $\sim 1\,\mathrm{g\,cm^{-3}}$ for the coolest known objects. If metals such as carbon, calcium, or sodium are present in these ultradense atmospheres, extreme broadening of atomic and molecular opacities can produce optical spectra that diverge significantly from blackbodies. We investigated how the combination of temperature and chemical composition can affect the perceived colours (chromaticity) of white dwarfs. While we found that most white dwarfs are similar in colour to blackbodies, we also demonstrate examples of known stars that would appear yellow, green, cyan, pink, or purple if viewed close enough for their stellar discs to be resolved. We examined the chromaticity distribution for the volume-limited 20 pc local sample of white dwarfs finding a median correlated colour temperature of ≈ 6800 K, establishing that, on average, white dwarfs are indeed white in colour. Finally we show how white dwarf spectral models can be used to generate colour-accurate images of their stellar discs as they would appear from up close.

Key words: Data methods – Visualizations – Colour science – White dwarfs.

1 INTRODUCTION

Stellar objects exhibit a wide variety of spectral energy distributions, depending on the physical properties of their outer layers, primarily including the temperature, density, and chemical composition of the stellar atmosphere. Consequently, these atmospheric conditions can influence how stars appear to a human observer, with sunlight and Sun-like stars having a white appearance, and hotter/cooler stars appearing pale blue/orange due to their approximate resemblance to blackbodies (J.-V. Harre & R. Heller 2021), though with the latter typically referred to as red in scientific contexts. These colours are accessible without the aid of telescopes, with bright stars such as Betelgeuse and Antares having noticeably redder hues than other nearby objects on the sky, and those like Sirius and Rigel appearing slightly bluer. However, the majority of stars are not visible to the naked-eye, including faint stellar objects like M dwarfs, brown dwarfs, and white dwarfs (the subject of this work). If these faint sources are viewed through telescopes, their colours will still not be accurately conveyed compared to if they were observed from up close, due to the reduced colour-discrimination of the eye under dark conditions (R. B. H. Tootell & S. Nasr 2020).

The chromatic diversity of faint stars can be approximately reflected in multichannel astronomical imaging, though these are typically not colour-accurate. For example, images from the Sloan Digital Sky Survey (SDSS; D. G. York et al. 2000; S. Alam et al. 2015; M. R. Blanton et al. 2017) map the *i*, *r*, and *g* bands on to the red, green, and blue (RGB) colour channels, respectively. However, the full range of human spectral sensitivity (see Section 2) covers only the *g* and *r* bands, limiting the colour-accuracy of such images.[1] Such false-colour images are often desirable for scientific analyses, with colours corresponding to wavelength ranges covering specific spectral features (which may also fall outside of the optical range entirely). While scientifically useful, false-colour images have the potential to mislead as to the true appearance of stars and other astrophysical bodies.

Establishing the perceived colours of astrophysical objects has received interest from the scientific community. Much focus has been given to main-sequence stars (P. Murdin 1981, 1987; T. P. Kohman 2005; M. Savino & N. F. Comins 2015; N. Cardiel et al. 2021; J.-V. Harre & R. Heller 2021) demonstrating their approximately blackbody colours. Brown dwarfs (A. Burrows 2001; A. Burrows et al. 2003; S. R. Cranmer 2021; O. Rering & B. Charnay 2025) have also been studied where their perceived colours are found to be magenta/violet,

★ E-mail: mark.hollands@warwick.ac.uk

[1]For example, a spectrum dominated by Hα emission will be covered by the SDSS *r*-band, and hence mapped to the green RGB channel, despite having a vivid red appearance in reality.

© The Author(s) 2026.
Published by Oxford University Press on behalf of Royal Astronomical Society. This is an Open Access article distributed under the terms of the Creative Commons Attribution License (https://creativecommons.org/licenses/by/4.0/), which permits unrestricted reuse, distribution, and reproduction in any medium, provided the original work is properly cited.

Downloaded from academic.oup.com/rasti/article/doi/10.1093/rasti/rzag069/8914458 by guest on 26 October 2026

primarily due to strong absorption from the Na-D doublet with highly broadened line wings in the optical (N. F. Allard et al. 2007). Interest in perceived colours is not limited to stellar objects, with P. G. J. Irwin et al. (2024) providing a recent reprocessing of Voyager 2 images of Uranus and Neptune, finding the latter to be a much less vivid shade of blue than previous images had shown, with both planets now appearing similar shades of pale blue-green. The perceptual colours of exoplanets have also been investigated (T. M. Evans et al. 2013), with P. Gao et al. (2021) using global circulation models of planetary atmospheres containing various aerosols, showing potentially stark differences in colour between their day and night sides. However, to our knowledge no particular attention has been paid towards the perceived colours of post–main-sequence objects such as white dwarfs, which is the focus of this work.

White dwarfs[2] are the dense stellar remnants left behind by the majority of main-sequence stars at the end of their lives. Their extreme properties can result in atmospheres that are significantly more dense compared to their main-sequence counterparts, particularly for the oldest stars in the white dwarf cooling sequence (P. M. Kowalski 2014; S. Blouin et al. 2018; P. Bergeron et al. 2022), resulting in broad-band opacities that can drastically alter their optical fluxes away from resembling a blackbody spectrum and providing ongoing challenges in their modelling (D. Saumon et al. 2022). It therefore stands to reason that the perceived colours of white dwarfs may also depart significantly from the blue, white, and orange exhibited by other kinds of stellar objects.

In this work we investigate the perceived colours of white dwarfs across a wide range of temperatures, compositions, and their resulting spectral types. In Section 2, we provide an introduction to the field of colour science, and describe the techniques required to convert astrophysical spectra to displayable colours on a typical computer monitor. In Section 3 we apply these techniques to a variety of observed and synthetic white dwarf spectra across the full range of white dwarf spectral subtypes, demonstrating their diverse range of perceived colours. We also apply these techniques to the volume-limited 20 pc local sample, showing the typical distribution of white dwarf colours. In Section 4, we show how colour-accurate images of white dwarfs can be generated from spectral models, where we provide examples for a variety of typical and atypical white dwarfs. Finally we present our conclusions in Section 5.

2 CALCULATING COLOURS FROM SPECTRA

While no stars other than the Sun can be observed close enough for their stellar discs to be visually resolved, the information required to determine their perceived colours is contained entirely within their optical spectra. Replicating these perceived colours from astrophysical spectra requires a model of the human visual system response to light (as a function of wavelength), a quantitative description of colour, and an understanding of how image and lighting technologies reproduce specified colours. These requirements are addressed by the field of colour science, which has become well established over the last century (T. Smith & J. Guild 1931; D. Judd & G. Wyszecki 1975; G. Wyszecki & W. Stiles 1982), particularly in its application to display technology (J. Foley et al. 1982; R. Hall 1988). In this section we give a basic introduction to the concepts used in the field of colour science which allow the conversion of a spectrum to the corresponding display colours.

Throughout this work, we work in the standard RGB colour space (sRGB, IEC 1999)[3] using the `python` package COLORPY.[4] This module contains routines for converting spectra into various colour spaces, conversions between colour spaces, and translation into display values to be used for computer displays.

2.1 Converting spectra to the XYZ colour space

The CIE (International Commission of Illumination/Commission Internationale de l'Éclairage) 1931 XYZ colour space (T. Smith & J. Guild 1931) is widely used in colour science and industry to quantify the subjective experience of colour, modelling the perception of colour in a linear additive way. Essentially this reduces the complexity of a spectrum down to three tristimulus values X, Y, and Z, by performing integrals (G. Wyszecki & W. Stiles 1982) of the form,

$$X = \int_{360}^{830} F_\lambda(\lambda) \cdot \bar{x}(\lambda)\, \mathrm{d}\lambda, \tag{1}$$

and symmetrically for $Y/\bar{y}(\lambda)$ and $Z/\bar{z}(\lambda)$, where λ is wavelength in nm, F_λ is flux density per unit wavelength, and $\bar{x}(\lambda)$, $\bar{y}(\lambda)$, and $\bar{z}(\lambda)$ are the CIE 1931 colour-matching functions.[5] Evidently, these integrals are analogous to calculating synthetic photometry of a spectrum within some bandpass in an astronomy context.

[2]Originally referred to as *faint white stars* (W. J. Luyten 1922) owing to the warm nature of the first few known objects, the term *white dwarf* was (to the best of our knowledge) coined by William Luyten in the Lick Observatory Bulletin XI.

[3]For an optimal viewing experience, computer monitors should be set to sRGB mode if available, and software used to lower the colour temperature for reducing eye strain should be disabled, or colours will not appear as intended. Ideally self-emissive displays should be used, as projected images will have their colours mixed with ambient light.

[4]http://www.markkness.net/colorpy/ColorPy.html
https://github.com/markkness/ColorPy

[5]Corrections are available to the 1931 colour-matching functions (D. B. Judd 1951; J. J. Vos 1978), and with more recently determined functions available from the CIE (A. Stockman & L. T. Sharpe 2000; D. MacLeod et al. 2006; F. Viénot et al. 2015). However, CIE 1931 remains ubiquitous for calibration of display technology, with the transformations to the sRGB colour space also specified in reference to CIE 1931. We therefore use the 1931 colour-matching functions for internal consistency.

Downloaded from academic.oup.com/rasti/article/doi/10.1093/rasti/rzag069/8914458 by guest on 26 October 2026

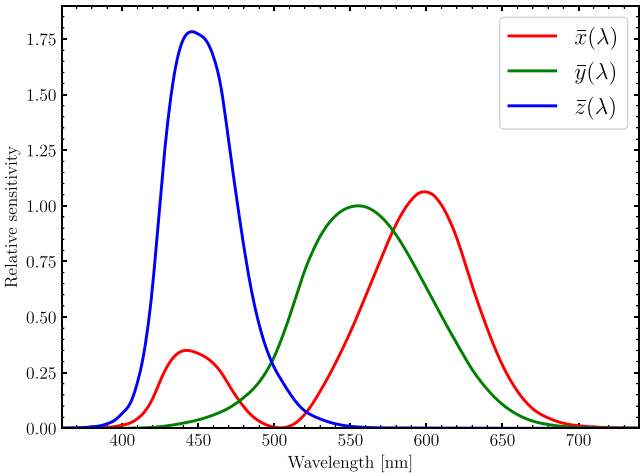

Figure 1. Colour matching functions for the 1931 CIE XYZ colour space. Integrating a spectrum over these curves results in the values of X, Y, and Z, which define the colour and intensity in the XYZ colour space.

The XYZ colour-matching functions (Fig. 1), were empirically determined to reflect the human visual system response to light under photopic vision over a 2 degree field of view from the eye centre (T. Smith & J. Guild 1931). It is important to note, however, that they do not directly reflect the individual cone responses, which are instead covered by the LMS colour space (Long/Medium/Short, e.g. A. Stockman & L. T. Sharpe 2000). Instead the CIE colour-matching functions are defined such that all three are non-negative, a flat spectrum in F_λ yields equal values of X, Y, and Z, and $\bar{y}(\lambda)$ is equivalent to the CIE photopic luminous efficiency function (the overall human visual response to perceived light intensity as a function of wavelength under photopic conditions) normalized to a peak of 1 (G. Wyszecki & W. Stiles 1982).

In COLORPY the function `xyz_from_spectrum` can be used on a spectrum to calculate XYZ values. Internally the integrals are performed using straight sums, assuming constant wavelength separation between flux values. Spectra must therefore be re-binned on to a linear wavelength-axis before this function is used.

While units of F_λ are not specified above, they are mostly unimportant here as all real stars have perceptual surface brightnesses (luminance, see Appendix A) far beyond the maximum output of any computer monitor. Instead we consider the component of colour independent of brightness, the chromaticity. To determine the chromaticity (G. Wyszecki & W. Stiles 1982), $X/Y/Z$ are normalized according to,

$$x = \frac{X}{X+Y+Z}, \qquad y = \frac{Y}{X+Y+Z}, \qquad z = \frac{Z}{X+Y+Z}. \tag{2}$$

As there are now only two degrees-of-freedom remaining, x and y can be used to define a 2D quantity that is independent of brightness, and is the primary coordinate system used to describe chromaticity. We show the full CIE x-y chromaticity diagram in Fig. 2. The chromaticity is analogous to a colour–colour diagram in astronomy contexts. However, rather than being defined in terms of logarithmic flux ratios, normalization by the total restricts the x, y values to the unit simplex.

The black curve around the edge of the filled region corresponds to monochromatic colours. Since all physical spectra are a linear combination of monochromatic colours, this curve bounds the space of all perceivable chromaticities. Outside of this region (but within the unit simplex) the ratios of $X/Y/Z$ are impossible given the CIE curves, for instance at long wavelengths > 700 nm, the ratio $\bar{x}(\lambda)/\bar{y}(\lambda)$ converges to about 2.8, and so there are no shades of red that involve illumination purely in X, but not in Y. Such impossible colours can only be experienced via direct stimulation of retinal cone cells (J. Fong et al. 2025).

The dotted triangle in Fig. 2 corresponds to the sRGB gamut, where the corners (filled squares) correspond to the sRGB primaries (see Section 2.2). Since this description of colour is linear, mixtures of the sRGB primaries can only correctly reproduce colours interior to the triangle. Consequently, chromaticities outside of the sRGB gamut cannot be accurately represented. For display purposes, we approximate these by clipping negative RGB values to zero.

The black curve emanating from the red corner is the blackbody/Planckian locus, and corresponds to the chromaticities of blackbody spectra. Ticks are from 2000 to 10 000 K in 1000 K steps. These ticks are not perpendicular to the Planckian locus in the xy-plane, as they instead correspond to isotherms in correlated colour temperature (see below). The 2000 K step appears at the boundary of the sRGB region, and so blackbody colours below that value cannot be accurately represented by an sRGB monitor, though all blackbodies above 2000 K can be. As no white dwarfs have convincingly been shown to have cooled to effective temperatures ($T_{\rm eff}$) below 3000 K (P. Bergeron et al. 2022; A. K. Elms et al. 2022; A. Caron et al. 2023), we expect most, if not all white dwarf chromaticities to fall within the sRGB gamut. The black circle at the end of the blackbody locus corresponds to $T \to \infty$, i.e. a pure Rayleigh–Jeans tail where $F_\lambda(\lambda) \propto \lambda^{-4}$. This gives $T \to \infty$ a chromaticity close to sky-blue, reflecting the λ^{-4} dependence of the Rayleigh-scattering cross-section.

Downloaded from academic.oup.com/rasti/article/doi/10.1093/rasti/rzag069/8914458 by guest on 26 October 2026

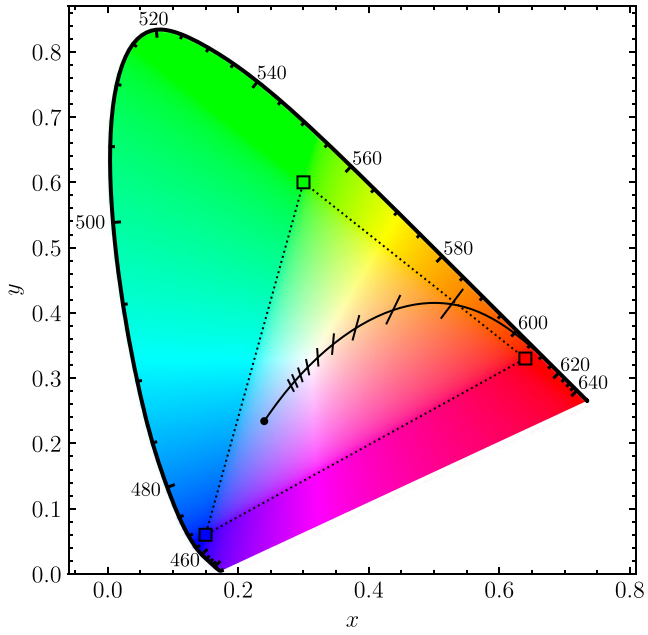

Figure 2. CIE 1931 chromaticity diagram in the x–y plane. The black curve bounding the filled region corresponds to monochromatic colours. The sRGB primaries are shown by the squares, defining a triangular region (dotted) which bounds the gamut of displayable chromaticities in the sRGB colour space. Colours outside of the triangle are therefore approximate. The black curve emanating from long wavelengths is the blackbody locus as a function of temperature, with isotherm ticks in correlated colour temperature shown from 2000 to 10 000 K in steps of 1000 K (from right to left).

While the CIE x–y chromaticity diagram remains widely used, a limitation of this colour space is that it is not perceptually uniform. In other words a small step of, say 0.01, within the x–y plane will result in a perceived chromaticity change that depends on the location within the plane and the direction of the step. To address this non-uniformity, other colour spaces with improved perceived uniformity have been introduced such as the 1960 Uniform Colour Space (UCS) (D. L. MacAdam 1937; CIE 1960). The UCS chromaticity values, u and v can be determined directly from the CIE 1931 x, y values, where

$$u = \frac{4x}{3 - 2x + 12y}, \quad v = \frac{6y}{3 - 2x + 12y}. \tag{3}$$

This form of chromaticity is used to define the correlated colour temperature, and is achieved by minimizing the Euclidean distance from a given point in the u–v chromaticity plane to the blackbody locus (the ticks in Fig. 2 were determined this way). This allows chromaticities near to the blackbody locus to be assigned a temperature, which we make use of in Section 3. Note that the correlated colour temperature is fundamentally different to the $T_{\rm eff}$, which is instead derived from the entire spectral energy distribution, though the two quantities may have similar values for spectra resembling blackbodies.

2.2 Conversion to linear RGB

A display colour space requires several key ingredients: the chromaticities of three display primaries, the chromaticity of a white point: that is to say the resulting mixture when all three primaries are at their maximum outputs, and a set of transfer functions which map the linear intensities of the primaries to display values.

In the sRGB colour space, the three primaries are labelled R, G, and B and have specified chromaticities $(x, y) = (0.64, 0.33)$, $(0.30, 0.60)$, $(0.15, 0.06)$, respectively (IEC 1999). Their linear intensities are given on a dimensionless scale 0 to 1, where 1 represents their maximum outputs. The white point is given by the standard illuminant D65 (close to a 6500 K blackbody spectrum), with a specified chromaticity $(x, y) = (0.3127, 0.3290)$ (IEC 1999). Finally, for an output of full-white, i.e. $R = G = B = 1$, the luminance, Y, is also specified to be 1. Collectively, these requirements can be used to derive a transformation matrix from XYZ to sRGB (and vice versa),

$$\begin{pmatrix} R \\ G \\ B \end{pmatrix} = \begin{pmatrix} 3.2410 & -1.5374 & -0.4986 \\ -0.9692 & 1.8760 & 0.0416 \\ 0.0556 & -0.2040 & 1.0570 \end{pmatrix} \cdot \begin{pmatrix} X \\ Y \\ Z \end{pmatrix}. \tag{4}$$

Even if the XYZ colours are normalized as per equation (2), after converting to sRGB (equation 4) the linear RGB values may not be at maximum intensity. Since the purpose of this work is to demonstrate the appearance of stars, we wish for colours to be displayed as brightly as possible, while preserving chromaticity. Therefore, throughout this work, we always rescale sRGB colours so that the brightest RGB channel has a linear value of 1. In order to convert these linear values to display colours, the final ingredient of the sRGB space, a transfer function must be applied.

Downloaded from academic.oup.com/rasti/article/doi/10.1093/rasti/rzag069/8914458 by guest on 26 October 2026

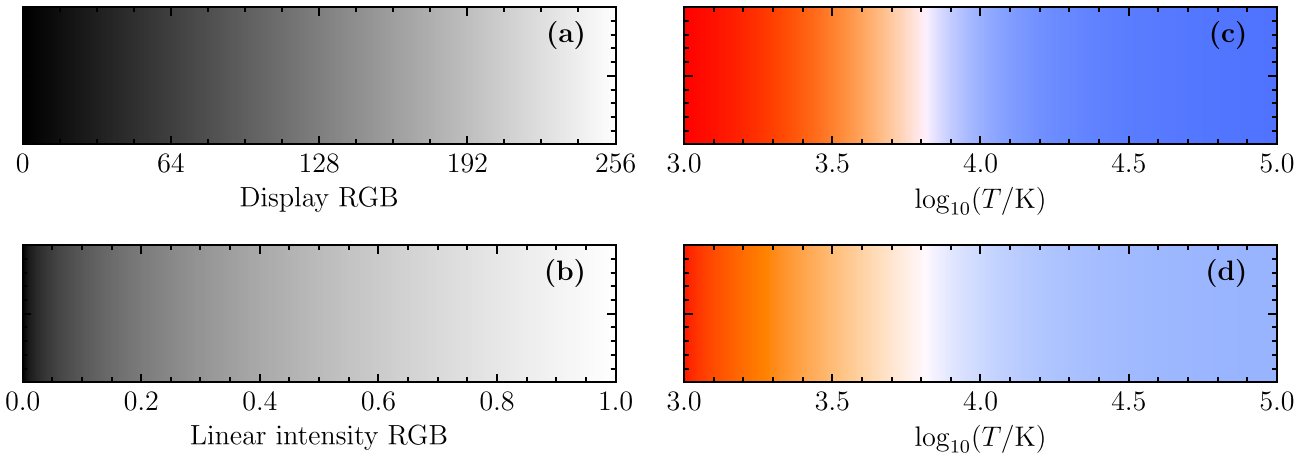

Figure 3. Comparison between not using (top) and applying (bottom) the sRGB OETF for greyscale (left) and blackbodies (right). (a) The greyscale is approximately perceptually linear, but due to the non-linear response of the human visual system, it is non-linear in intensity. (b) The greyscale is linear in intensity, but appears perceptually non-linear. Blackbody colours appear overly saturated when an OETF is not applied (c) compared with applying the sRGB OETF (d). Note that temperatures below $\simeq$ 2000 K ($\log_{10}(T/\mathrm{K}) \simeq 3.3$) are outside of the sRGB gamut and so are approximated. All colours are scaled to the maximum displayable brightnesses.

2.3 Transfer functions

In the sRGB colour space, 8-bit displayable values (per colour channel) are given as integers in the range 0 to 255. One might naïvely assume that conversion from linear RGB values is as simple as,

$$I_{\mathrm{display}} = \mathrm{round}(255 I_{\mathrm{linear}}), \tag{5}$$

where I are one of the RGB channels. However, the human eye does not respond linearly to light intensity, and neither do pixel intensities as a function of the 0–255 display values. Instead, an opto-electronic transfer function (OETF) is used to map linear light values to a displayable range, and an electro-optical function (EOTF) is used to perform the inverse. Historically, cathode-ray tube displays had intensities with a power-law (gamma-function) dependence on the voltage V,

$$I \propto V^{\gamma}, \tag{6}$$

where typically $\gamma = 2.2$. Instead of a pure gamma function, sRGB uses a piecewise function (IEC 1999), which approximates a gamma function with $\gamma = 2.2$, but has a small linear segment for low intensities, avoiding a vertical slope at the origin as with a pure gamma OETF. For input intensities I and output values V, both in the range 0–1, the OETF is given by

$$V = \begin{cases} 12.92I & \text{if} \quad I \leq 0.0031308 \\ 1.055 I^{1/2.4} - 0.055 & \text{otherwise,} \end{cases} \tag{7}$$

and is applied to all three RGB channels. After equation (7) has been applied to the linear values, then equation (5) is used to convert to the display values in the range 0–255.

We now demonstrate visually the difference applying the sRGB OETF makes when used or not (Fig. 3). In the panels (a) and (b), we show simple greyscales. In panel (a), equation (7) is not used and each value along the x-axis corresponds to one of the display values in the range 0–255. This scale appears perceptually close to linear, despite the non-linear scale in brightness. This is of course useful for displaying shades with a large dynamic range in intensity. In panel (b), the intensity is instead linear on the range 0–1, but appears perceptually non-linear with a rapid perceived change at low values, demonstrating the human eye's improved discrimination between dark shades compared to bright ones.

In the right panels of Fig. 3, we show blackbody colours without (c) and with (d) the sRGB OETF (equation 7) applied before quantizing with equation (5). In both panels colours are normalized so that the brightest of the three RGB channels is at its maximum (1.0 on the linear scale and 255 on the display scale). The temperature scale ranges from 1000 to 100 000 K (logarithmically) showing the expected transitions through red, orange, white, and blue colours. In (c), the uncorrected case (equivalent to applying a gamma OETF with $\gamma = 1$), the cool temperatures are much redder than real blackbodies, and at hot temperatures are much bluer than expected, as the outputs between the channels do not have the correct ratios. These oversaturated colours resemble those found by J.-V. Harre & R. Heller (2021) who did not apply an OETF in their analysis of main-sequence stars.

2.4 Examples

To summarize, the process to go from a stellar spectrum to an sRGB colour is as follows.

Downloaded from academic.oup.com/rasti/article/doi/10.1093/rasti/rzag069/8914458 by guest on 26 October 2026

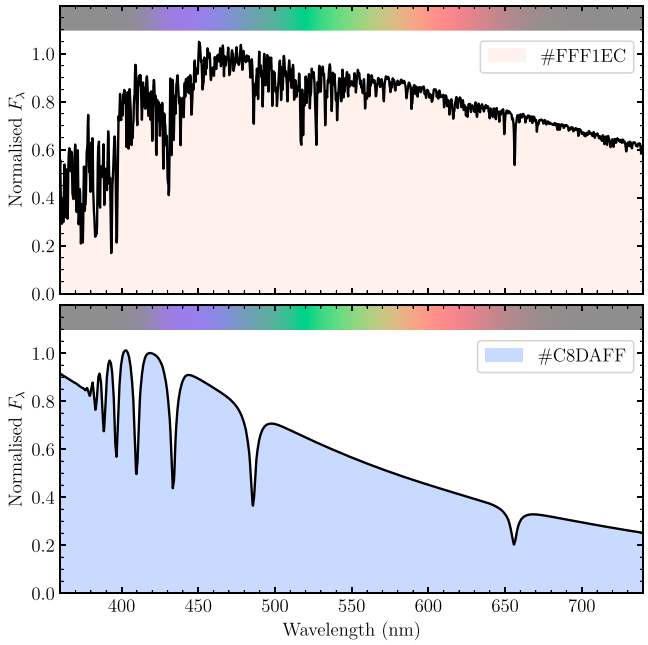

Figure 4. A solar model spectrum (top) and a 10 000 K hydrogen atmosphere white dwarf model spectrum (bottom) are shown, under-filled with their perceived colours. Their corresponding sRGB hex codes are shown in the top right of each panel. Both models are convolved to a full width at half maximum of 5 Å for clarity. The bars above each panel approximate the appearance of monochromatic emission at constant intensity, though mixed with the minimal amount of grey to move all colours in-gamut.

(i) Integrate the spectrum over the CIE XYZ colour-matching functions using equation (1) to determine the values of X, Y, and Z. If needed, normalize using equation (2) to determine the chromaticity in terms of x and y.

(ii) Use the transformation matrix in equation (4) to convert XYZ values to linear sRGB in terms of R, G, and B, normalizing the brightest component to 1.

(iii) Apply the sRGB OETF from equation (7) and quantize with equation (5) to convert to displayable sRGB values in the 0–255 range.

With these necessary ingredients specified above, we conclude this section with two examples for a Solar model, and a pure hydrogen 10 000 K white dwarf model spectrum, with the results shown in Fig. 4.

The Solar model in the top panel of Fig. 4 was taken from the BT-NextGen (AGSS2009) grid (P. H. Hauschildt et al. 1999) with $T_{\rm eff} = 5800$ K, $\log g = 4.5$, and solar metallicity. Integrating over the colour-matching functions, and normalizing to $Y = 1$, we found ($X = 0.974, Y = 1, Z = 1.024$), with a corresponding chromaticity of ($x = 0.325, y = 0.334$). Converting to linear sRGB, and scaling to the brightest component, we arrive at ($R = 1, G = 0.878, B = 0.840$). Applying the sRGB transfer function and quantizing, we found display values of ($R = 255, G = 241, B = 236$) (the corresponding hexadecimal value is shown on the figure). While the Sun is ostensibly 'white' in colour, the model correlated colour temperature (≈ 5870 K, slightly higher than its $T_{\rm eff}$) is somewhat lower than the 6500 K sRGB white point, and so appears marginally redder and fainter than the figure background.

The white dwarf model is of a pure hydrogen atmosphere with $T_{\rm eff} = 10\,000$ K at $\log g = 8$ (see Section 3.1 for details). Following the same procedure, we found ($X = 0.960, Y = 1, Z = 1.496$) in XYZ space, with a chromaticity of ($x = 0.278, y = 0.289$). The normalized linear sRGB values were found to be ($R = 0.580, G = 0.704, B = 1$). Converting to display sRGB, we then found display values of ($R = 200, G = 218, B = 255$). Compared to the Solar model, the X/Y ratios are quite similar as they both approximately sample their Rayleigh–Jeans tails. However the Z/Y ratio is much higher for the white dwarf due to the greater proportion of flux radiated in the blue end of the optical. Consequently, the white dwarf appears pale blue, as expected for stars in the region of $T_{\rm eff} = 10\,000$ K.

Of course the surfaces of both example stars are enormously brighter than it is possible to show here, but with the chromaticity of these stars depicted as accurately as possible. As these model spectra represent the flux integrated over their stellar discs, they can instead be interpreted as the colour they would illuminate a white surface some distance from the stars, i.e. a surface that scatters all wavelengths equally.

3 COLOURS OF WHITE DWARFS

3.1 Pure hydrogen and helium atmospheres

The simplest white dwarfs are those with near pure hydrogen or helium atmospheres. For pure hydrogen atmospheres, their optical spectra are dominated by hydrogen lines above $T_{\rm eff} \simeq 5000$ K giving them the spectral type DA (E. M. Sion et al. 1983). Similarly, pure

Downloaded from academic.oup.com/rasti/article/doi/10.1093/rasti/rzag069/8914458 by guest on 26 October 2026

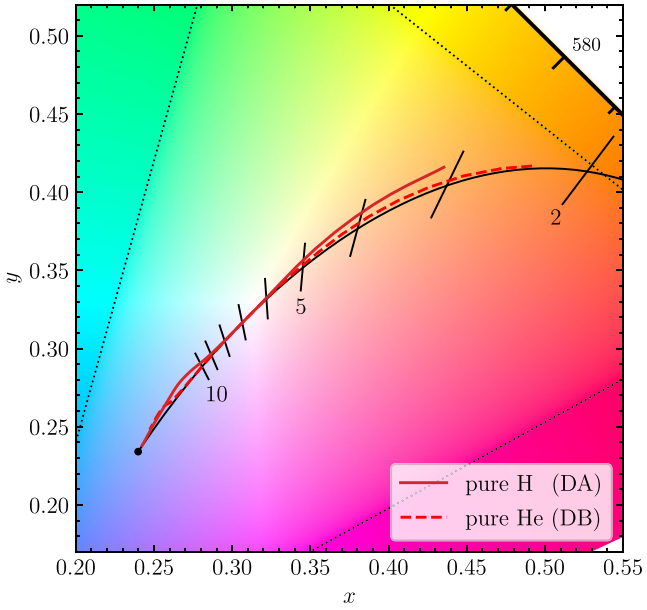

Figure 5. CIE chromaticity diagram, zoomed-in compared with Fig. 1, and overlaid with tracks for pure hydrogen (DA) and pure helium (DB) white dwarf model colours as a function of $T_{\rm eff}$, all with $\log g = 8$. The black curve corresponds to the blackbody locus as before, with ticks indicating correlated colour temperature and their labels in kK.

helium atmosphere white dwarfs exhibit lines from neutral helium from around 11 000 to 40 000 K giving them the spectral type DB (above this range He II lines dominate with spectra designated DO). At lower temperatures, both hydrogen and helium are insufficiently excited to show spectral lines, resulting in continuum spectra classified as DCs.

To visualize the colours of these simpler white dwarfs, we used grids of models with surface gravity, $\log g$, fixed to 8, and $T_{\rm eff}$ as the only free parameter. Model spectra such as these are free from problems such as poor flux-calibration which could make observed data yield incorrect colours. We made use of the Tremblay model atmospheres, which include 3D and non-local thermodynamic equilibrium (NLTE) effects (P.-E. Tremblay et al. 2011, 2013), and include a recent correction to the H_3^+ partition function relating to nuclear spin degeneracy. More recently these models have been adapted to compute 3D helium-rich atmospheres (E. Cukanovaite et al. 2018, 2019, 2021). Here we focus on their pure helium grid.

For hydrogen atmospheres, we computed colours for models spanning $T_{\rm eff} = 3000$ to 140 000 K with step-size increasing as a function of $T_{\rm eff}$. For helium atmospheres, the model grid instead spanned 3000 to 40 000 K. The model tracks for both pure hydrogen and pure helium are shown in the CIE chromaticity diagram in Fig. 5. The chromaticity, linear sRGB, and display sRGB hex codes are tabulated in Tables C1 and C2, and figures for a subset of those spectra are shown in Figs B1 and B2.

From the tracks in Fig. 5, we see that in general both pure hydrogen and helium atmospheres are well approximated by blackbody colours. However DAs do show some small deviations at the highest and lowest temperatures. For correlated colour temperatures above $\simeq$ 9000 K, there is a slight deviation to higher y values which vanishes for even higher colour temperatures. We found this is due to the emergence and disappearance of the Balmer lines in the optical, particularly Hγ. While the Balmer jump similarly emerges and vanishes in this $T_{\rm eff}$ range, it has less of an effect on the chromaticity due to the diminished sensitivity of the human-eye below 400 nm (Fig. 1).

At correlated colour temperatures below about 5000 K the hydrogen models again begin to deviate away slightly from the blackbody colours towards higher y values. This can be attributed to two reasons: first, the formation of hydrogen molecules at low $T_{\rm eff}$ where collisions between H_2 and other neutral particles (H_2-H_2 or H_2-H; A. Borysow et al. 2001) can induce a temporary H_2 dipole moment, known as collision induced absorption (CIA). Initially the broad opacity from CIA only has a measurable effect on the near infrared, only subtly affecting optical fluxes. At even lower $T_{\rm eff}$, the CIA becomes sufficiently strong to be visible at optical wavelengths, where it is apparent at the reddest wavelengths of the $T_{\rm eff} = 3000$ K model in Fig. B1. Secondly, neutral broadening of the hydrogen Lyα line in the ultraviolet, affects the blue end of the optical at low $T_{\rm eff}$ (P. M. Kowalski & D. Saumon 2006). The broadening of Lyα arises due to interaction with other particles (protons, electrons, H, H_2) in the plasma (which becomes increasing dense at low $T_{\rm eff}$), altering both the hydrogen energy levels and dipole moments. At the lowest $T_{\rm eff}$, Lyα broadening becomes so extreme that its red wing extends into the blue end of the optical, depressing flux in this region (R. D. Rohrmann et al. 2011).

By contrast, the pure helium track closely follows the blackbody locus in Fig. 5. At low $T_{\rm eff}$ the optical opacities are almost grey, arising predominantly from He^- free–free absorption: due to the absence of hydrogen in these models, no broad Lyα is present, nor the CIA opacities mentioned above. Inspecting the models in Fig. B2 it is indeed clear that the featureless spectra of pure helium atmospheres resemble blackbodies (N. Suzuki & M. Fukugita 2018; A. Serenelli et al. 2019) for the $T_{\rm eff} \leq 10\,000$ K models. Another noteworthy point for our pure helium models is that while they have chromaticities closely resembling blackbodies, their $T_{\rm eff}$ appears higher than the

Downloaded from academic.oup.com/rasti/article/doi/10.1093/rasti/rzag069/8914458 by guest on 26 October 2026

corresponding colour temperature. This is most easily seen at the cool end of the helium track in Fig. 5, with a corresponding $T_{\rm eff}$ of 3000 K, but at a correlated colour temperature of about 2400 K. For DAs the difference is smaller and inverted: with the $T_{\rm eff} = 3000$ K end of the track having a colour temperature of about 3100 K instead. A final important point of interest is that both model tracks shown in Fig. 5 are fully contained well within the sRGB gamut, indicating that in general, white dwarfs chromaticities can be accurately represented by sRGB displays.

3.2 Cool, mixed atmosphere (IR-faint) white dwarfs

In reality, white dwarfs with effectively pure helium atmospheres are rarely encountered, with at least some level of trace hydrogen usually present. This hydrogen provides an additional source of free electrons, and introduces other opacity sources that are not present in pure helium. Since hydrogen is present, the Lyα line is once again present in the ultraviolet, but now also broadened by neutral helium (B. T. Gänsicke et al. 2018; N. F. Allard et al. 2020). Another important opacity source becomes prevalent at low $T_{\rm eff}$ (< 5000 K), where trace hydrogen introduces two new forms of CIA from H-He and H_2-He, the latter of which can become particularly strong for abundances of $\log({\rm H/He}) \simeq -3$ dex (S. Blouin et al. 2017). These CIA features can severely depress flux in the near-infrared earning them the classification IR-faint[6] (P. Bergeron et al. 2022). In the most extreme cases the CIA can extend far into the optical, resulting in white dwarfs with optical spectra peaking at blue wavelengths, despite their low temperatures.

IR-faint white dwarfs are among the most challenging degenerate stars to model in terms of their spectra (P. Bergeron & S. K. Leggett 2002), as their transparent atmospheres reach liquid densities requiring advanced equation-of-state models (S. Blouin et al. 2024). Even the most advanced white dwarf model atmosphere codes struggle to fully model their ultrabroad spectral features, including those we have access to. To avoid the limitations of our models causing incorrect calculated colours, for IR-faint white dwarfs we have opted to use optical spectra from SDSS.

To ensure problematic flux calibrations of SDSS spectra did not adversely influence our colour calculations, we adopted the method from M. A. Hollands et al. (2017) for correcting SDSS spectral fluxes using their photometry. The SDSS spectra fully cover the wavelength ranges for the *g*, *r*, and *i* bands from SDSS imaging. We therefore calculated synthetic photometry from SDSS spectra for these three, minimizing the magnitude differences by iteratively re-scaling the spectra by first-order polynomials in magnitude-space (exponential in flux-space) as a function of wavelength. In M. A. Hollands et al. (2017), we found that this approach worked well, where the fitted models to DZ spectra agreed with the other SDSS photometric bands (*u* and *z*) that are not fully covered by the SDSS spectra. In some cases, subtraction of O I and Na I sky-emission lines is poor due to the faintness of some of the objects, and so we interpolated over the wavelengths for those lines to remove their influence on our colour calculations. Additionally, SDSS spectra taken before data release 9, when the SDSS spectrograph was upgraded to the BOSS instrument (K. S. Dawson et al. 2013), only extend as far bluewards as 380 nm. While the CIE colour-matching functions are tabulated down to 360 nm, by 380 nm the $\bar{z}(\lambda)$-curve (Fig. 1) sensitivity is already negligible, and only 0.05 per cent of its integrated area lies between 360 to 380 nm. This wavelength range is therefore ultimately unimportant for calculating accurate chromaticities.

We selected 15 IR-faint white dwarfs (Table C3) from M. A. Hollands et al. (2017) and P. Bergeron et al. (2022) with peculiar spectra (Fig. B3) for which we determined their perceived colours and locations in the CIE chromaticity diagram (Fig. 6). These stars were chosen to demonstrate the range of chromatic diversity for objects with extreme CIA affecting their optical colours, and therefore should not be considered an unbiased or representative sample of IR-faint white dwarfs in general. Despite being ostensibly cool stars, most objects considered have correlated colour temperatures between 5000 and 10 000 K, demonstrating the strong effect that the CIA opacity has on their emergent flux (compared to pure helium) and thus the chromaticity. However, this does not mean that IR-faint stars simply have colours resembling warmer blackbodies, instead having chromaticities shifted upwards in the *y*-direction compared to the blackbody locus. From Figs 6 and B3 it is seen that the IR-faint white dwarfs with the lowest *x* values occupy the cyan part of the chromaticity diagram. In Fig. B3, this is perhaps most readily apparent for WD J0039+3035 and WD J1403+4533 (full coordinates given Table C3), which both show relatively high signal-to-noise ratio (S/N) spectra and prominent cyan colours. Even more extreme is WD J1251+4403 which appears visually blue with a correlated colour temperature of 12 700 K, though we note its low S/N spectrum. The IR-faint white dwarfs with correlated colour temperatures near 5000 K appear a pale yellow colour instead. By contrast WD J0854+3503 shows relatively little CIA in the optical, and therefore has an orange colour more befitting its $T_{\rm eff}$. In any case, IR-faint white dwarfs demonstrate that the broad opacities encountered in these ultradense atmospheres result in stars that are far from blackbodies at the same $T_{\rm eff}$.

3.3 Carbon-rich white dwarfs

White dwarfs with spectra dominated by carbon features are classified as DQs (E. M. Sion et al. 1983). The carbon is generally understood to be dredged up core material, mixed into a convective outer helium layer (D. Koester et al. 1982; G. Fontaine et al. 1984). For hot DQs a merger origin is also possible (P. Dufour et al. 2007) resulting in carbon-dominated atmospheres. The most common case, and the one

[6]Such stars had previously been referred to as ultracool white dwarfs, a term reserved for $T_{\rm eff} < 4000$ K objects. However, P. Bergeron et al. (2022) showed that corrections to H_2-He CIA and He^- free–free opacities results in higher measured $T_{\rm eff}$.

Downloaded from academic.oup.com/rasti/article/doi/10.1093/rasti/rzag069/8914458 by guest on 26 October 2026

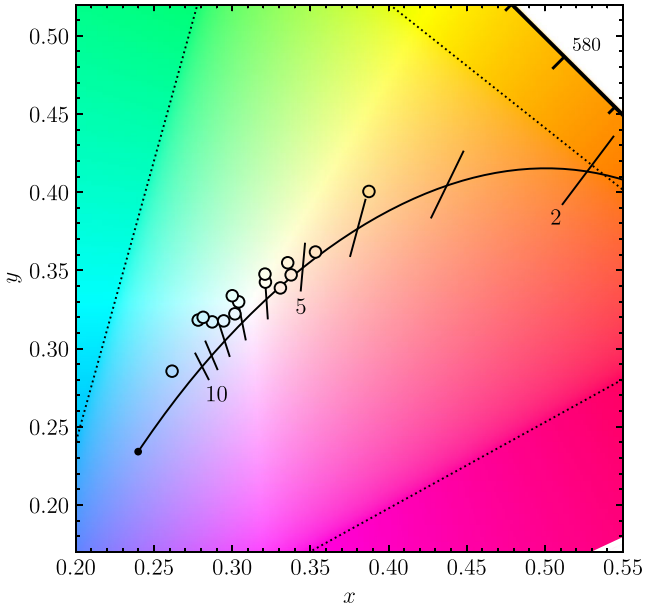

Figure 6. CIE chromaticity diagram, zoomed-in compared with Fig. 1, showing a selection of IR-faint white dwarfs with optical flux-peaks shifted bluewards. The most extreme objects appear at cyan chromaticities.

we predominantly examine here, is for cool white dwarfs where helium features have practically vanished and the dominant carbon features are from C_2 molecules. These molecules form wide absorption bands across the optical known as the Swan bands, and are also visible in carbon stars (P. F. Bernath 2009). As these bands occur at wavelengths the human eye is most sensitive to, it stands to reason that the perceived colours of DQs could be dramatically different from blackbodies.

For $T_{\rm eff}$ below $\simeq$ 6500 K where photospheric densities of helium-rich atmospheres exceed $\simeq 0.15\,{\rm g\,cm^{-3}}$ (S. Blouin & P. Dufour 2019), the Swan bands become distorted and shifted bluewards (P. B. Hall & A. J. Maxwell 2008; P. M. Kowalski 2010). Further distortion may also result from magnetic fields (I. Bues 1999). These 'peculiar' DQs are classified DQpec to distinguish their unusual spectra (G. D. Schmidt et al. 1995). Such spectra pose a modelling challenge to state-of-the-art white dwarf atmosphere codes, with the most extreme examples only approximately replicated (S. Blouin & P. Dufour 2019). For this reason we again opt to use observed spectra from SDSS, applying the same correction to flux calibration as in Section 3.2.

We drew a selection of 10 DQpec white dwarfs from S. Blouin & P. Dufour (2019), where most of their objects of study have SDSS spectra. We also selected 26 more DQ and DQpec white dwarfs with SDSS spectra (S. O. Kepler et al. 2016) to complement these, bringing the total to 36. As with IR-faint white dwarfs this is not meant to be a representative, unbiased sample of DQs, but is intended to demonstrate the wide range and most extreme white dwarf colours that are possible. As with the other white dwarf classes we show the DQ colours in a zoomed-in chromaticity diagram in Fig. 7. The spectra themselves are shown in Figs B4 and B5, and their colour information is listed in Table C4.

In contrast with the IR-faint white dwarfs the DQs are shifted below and to the right of the blackbody locus in the chromaticity diagram. As with the previous spectral classes, all DQ white dwarf colours are contained with the sRGB gamut indicating they can be replicated accurately. The warmest of the selection are shades of blue close to blackbodies, such as WD J0859+3257 (Fig. B4) which shows a mix of spectral features from atomic and molecular carbon. For slightly lower correlated colour temperatures, a few DQs appear as pale shades of purple instead, such as WD J0136+2004. Below colour temperatures of about 7000 K, most objects show minor to extreme distortion of the Swan bands (DQpec), and are instead indicated by squares in Fig. 7. These objects mostly exhibit various shades of pink depending on their temperature and the strength of the Swan bands (Figs B4 and B5). Some notable DQpec include the magnetic objects (G. D. Schmidt et al. 2003) WD J1113+0146 which has highly distorted Swan bands, and WD J1333+0016 which is particularly far from the blackbody locus ($x = 0.387, y = 0.306$) giving it a more vivid pink hue than other similar objects. At cool temperatures with lower carbon abundances we also found DQpec with peach colours instead, such as WD J1803+2320 (Fig. B5).

A standout DQpec is WD J1011+2845 (also known as LHS 2229 or LP 315−42). This nearby white dwarf (14.73 ± 0.01 pc away; M. W. O'Brien et al. 2024), is estimated to have a low $T_{\rm eff}$ of 4300 K (S. Blouin & P. Dufour 2019), and has a spectrum (Fig. B5) of deep and distorted Swan bands, which likely arises from a combination of atmospheric density (S. Blouin & P. Dufour 2019) and a strong magnetic field (G. D. Schmidt et al. 1999). As a result, the majority of its visible flux is restricted to wavelengths > 600 nm, with wavelengths from 400 to 600 nm greatly suppressed. The resulting colour is a unique hue of deep salmon-pink. Like WD J1333+0016 (which has similarly shaped Swan bands, but emits a greater fraction of flux below 450 nm) it also resides far from the Planckian locus in Fig. 7, making it one of the most visually distinct objects in this analysis, and likely the reddest star known in terms of perceived colour. White dwarfs such as

Downloaded from academic.oup.com/rasti/article/doi/10.1093/rasti/rzag069/8914458 by guest on 26 October 2026

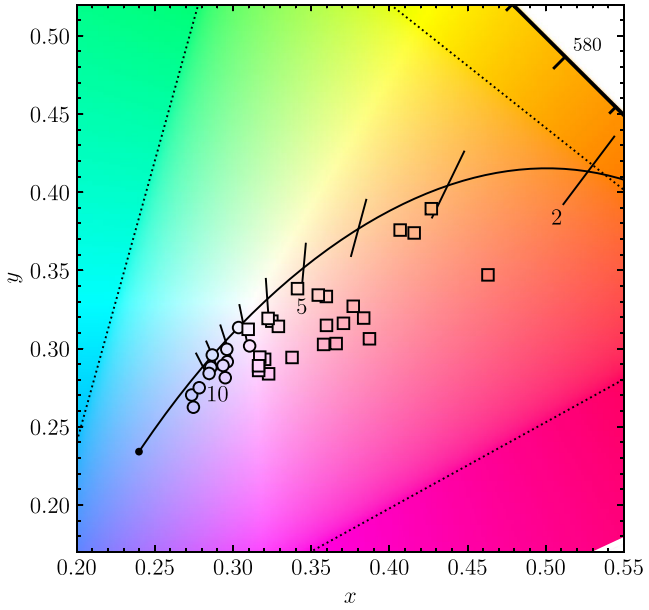

Figure 7. CIE chromaticity diagram, zoomed-in compared with Fig. 1, showing a selection of DQs, both normal (circles) and peculiar (squares) DQ subtypes. Generally the DQs appear below the blackbody-locus, giving them pink and purple colours.

WD J1011+2845 clearly demonstrate the effect that broad-band opacity sources such as molecular bands can have on their atmospheres, making them visually different from the orange, white, and blue chromaticities of main-sequence stars and blackbodies.

3.4 Cool metal-rich white dwarfs

When metal lines (excluding carbon) appear in the spectra of white dwarfs a Z is added to their spectral classification. These metals are now understood to originate from the external pollution of the white dwarf atmosphere by rocky debris from its planetary system, i.e. asteroids (M. Jura 2003; B. Zuckerman et al. 2007, 2010) and comets (S. Xu et al. 2017; J. T. Williams et al. 2025; S. Sahu et al. 2025), with almost 2000 such systems known at the present time (J. T. Williams et al. 2024). Warm white dwarfs enriched with planetary traces are classified DAZ or DBZ when metal lines are secondary to hydrogen or helium, respectively, though their narrow metallic absorption lines have little effect on their perceived colours compared to metal-free DAs and DBs. However, once helium-rich white dwarfs become sufficiently cool ($T_{\rm eff}$ < 11 000 K), helium lines are no longer visible giving them the classification DZ. Their atmospheres become increasing transparent and dense with decreasing $T_{\rm eff}$ (reaching up to 1 g cm^{-3}), causing the strongest metal lines to become extremely broad (hundreds to thousands of Å), and in some cases asymmetric (N. F. Allard et al. 2016b). These highly broadened metal lines therefore have the potential to alter their chromaticities away from blackbodies in a comparable way to carbon in cool DQs (Section 3.3).

Such lines cannot be modelled under the impact approximation with standard Lorentzian profiles (N. Allard & J. Kielkopf 1982), and must instead be given a bespoke treatment using the unified line shape theory (N. F. Allard et al. 1999). The unified theory considers the effect of perturber distance (in this case helium) on both the energy levels and dipole moments of the atom/ion undergoing a transition, allowing the line profile to be determined as a function of temperature and perturber density. For DZs, unified profiles are employed for the strongest lines where accurate modelling of the line core and wings are both important, specifically Mg II h+k (≃ 2800 Å), the Mg I resonance line (≃ 2853 Å) and b-triplet (≃ 5170 Å), the Ca II H+K lines (≃ 3950 Å), the Ca I resonance line (≃ 4227 Å), and the Na I D-doublet (≃ 5890 Å). Calculations for these (N. F. Allard & Alekseev 2014; N. F. Allard et al. 2016b, a; M. A. Hollands et al. 2017) are now present in white dwarf atmospheric codes for modelling DZs (e.g. M. A. Hollands et al. 2017; S. Blouin et al. 2018; S. Coutu et al. 2019; A. Kawka et al. 2021), and are used to varying degrees in the DZ models we show here.

We selected 33 DZ white dwarfs from M. A. Hollands et al. (2017), a sample of 231 DZs from the SDSS, for which we had already computed model spectra using the 1D LTE Koester model atmosphere code (D. Koester 2010). Our 33 object selection was chosen to include examples of typical DZs with strong metal lines across a wide range of temperatures (4000 < $T_{\rm eff}$ < 9000 K), as well as white dwarfs that we found had particularly unusual colours. While there have been numerous improvements to the Koester model atmosphere code since these models were first published, it is unnecessary to refit the spectra: As long as the models provide reasonable matches to both the optical spectra and photometric fluxes then the calculated chromaticities will remain accurate. We therefore used updated models only where already available from more recent analyses (i.e. WD J0956+5912, WD J1038−0036, and WD J1535+1247; M. A. Hollands et al. 2022) or for objects where further modelling was required in Section 4 (WD J0744+4649, WD J0851+1543, and

Downloaded from academic.oup.com/rasti/article/doi/10.1093/rasti/rzag069/8914458 by guest on 26 October 2026

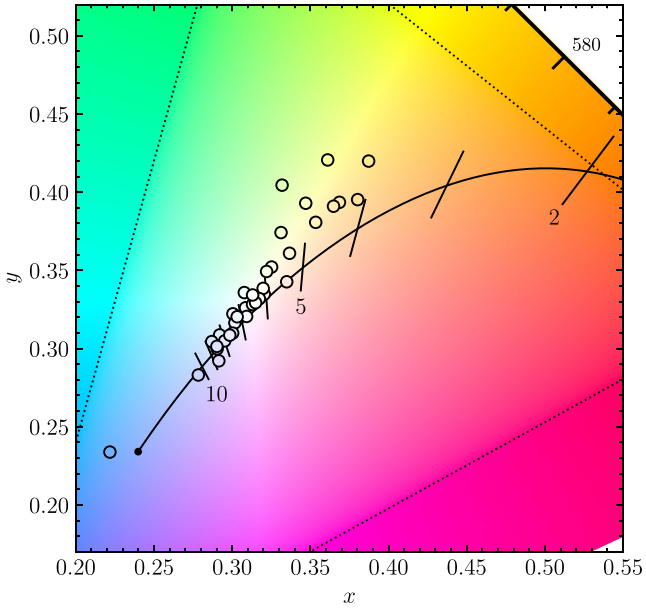

Figure 8. CIE chromaticity diagram, zoomed-in compared with Fig. 1, showing our sample of 36 DZs. Towards low temperatures most of the DZs appear above the blackbody locus, with WD J1330+6435 appearing green, and WD J2356−2054 a vivid blue.

WD J0916+2540). We supplemented the above 33 DZs with three more objects with particularly intriguing spectra: WD J1330+6435 and WD J1824+1213 from M. A. Hollands et al. (2021), and WD J2356−2054 from S. Blouin et al. (2019a), bringing the total selection to 36. These stars were also modelled with an up-to-date version of the Koester atmosphere code. The 36 selected objects are shown in a chromaticity diagram (Fig. 8), with their points filled with their corresponding colours. All objects are interior to the sRGB gamut indicating that the colours of DZs can be displayed accurately, as with other white dwarf spectral classes. Their spectra are shown in Figs B6 and B7, and their colour information is listed in Table C5.

There is a moderate degree of scatter in the model chromaticities at all temperatures (Fig. 8), though for the warmer objects with correlated colour temperatures above 6000 K, this scatter is mostly around the blackbody locus. At cooler temperatures the white dwarfs move towards higher y-values where all objects with correlated colour temperatures below 5000 K sit above the blackbody locus. Consequently, the colours of these stars exhibit a particularly diverse range of hues. We discuss some of the more uniquely interesting objects below.

WD J1330+3029 despite its strong metal lines has a results in a chromaticity that almost exactly matches the sRGB white point, with a hex code of #FFFEFF. WD J0744+4649 shows strong absorption at blue wavelengths from pressure broadened resonance lines of Ca I and Ca II (Fig. B6). It also exhibits a deep and unresolved Na I doublet at 589 nm at orange wavelengths, but does not show much absorption from Mg at 517 nm (green wavelengths), as with most DZs. These abundances led M. A. Hollands et al. (2018a) and J. H. D. Harrison et al. (2021) to conclude the accreted planetesimal contained a moderate amount of crust-like material. As a result of these absorption features (particularly Ca which absorbs most of the flux below 460 nm) its perceived colour is not orange, but yellow. Other white dwarfs such as WD J0916+2540 (Fig. B6) are also seen to be yellower than is possible for blackbodies, but still contain some degree of orange.

WD J1646+2238 (Fig. B7) is markedly different from the other DZs, having a larger than typical amount of trace hydrogen of $\log(\mathrm{H/He}) = -1.8$, which results in its continuum slope being shallower than other DZs of the same $T_{\rm eff}$, increasing the degree of red flux. As a result, it has a pale-pink colour, though not as vibrant as found for the DQs in Section 3.3.

The most surprising colour comes from WD J1330+6435. This object has been analysed by B. C. Kaiser et al. (2021) and M. A. Hollands et al. (2021), due to the presence of lithium in its spectrum (Fig. 8), with another recent analysis by S. Blouin et al. (2019a). For the analysis in M. A. Hollands et al. (2021), we lacked data for unified profiles for the Na doublet at that time, instead using inadequate Lorentzian profiles that led to a cooler solution than B. C. Kaiser et al. (2021). With unified profiles for Na now in hand we find similar model parameters to B. C. Kaiser et al. (2021) with $T_{\rm eff} = 4240$ K, $\log g = 8.22$ dex, $\log(\mathrm{Li/He}) = -10.6$, $\log(\mathrm{Na/He}) = -8.7$, and $\log(\mathrm{Ca/He}) = -8.8$. Due to the strong, broad Na I doublet absorbing orange wavelengths, and Ca absorbing at violet wavelengths, the resulting peak in flux occurs around 500 nm, giving WD J1330+6435 a perceived colour of chartreuse green (Fig. B7). To our knowledge, no other stars of any kind have been claimed to exhibit a green hue, making white dwarfs so far the only known way to produce a green star. We note that the spectrum of WD J1330+6435 is somewhat noisy, and so it is conceivable that its chromaticity may differ slightly in reality. However, our previous model from M. A. Hollands et al. (2021) using a standard Lorentzian profile shows a similar hue (#EAFFA1), giving us confidence in the green appearance of WD J1330+6435.

Downloaded from academic.oup.com/rasti/article/doi/10.1093/rasti/rzag069/8914458 by guest on 26 October 2026

WD J1330+6435 is not the only green object in our sample of 36, though it is the most vivid: WD J0851+1543 (Fig. B6), and WD J1351+2645 (Fig. B7) also both appear green but are much paler than WD J1330+6435, where their green hues can be explained by strong Ca II at blue wavelengths, and their steep Rayleigh–Jeans tails in the red. For WD J0851+1543, while its colour is pale, the hue is further from yellow than the other objects (between sRGB green and cyan). Since the fit to this star was based on a higher S/N spectrum, the green status of WD J0851+1543 can be claimed reliably.

We also investigated WD J1644+1234, another Li-rich white dwarf analysed by B. C. Kaiser et al. (2021). While we do not have access to their data, we were able to compute a model with the same parameters. Our model showed a similar greenish colour (#EAFFC5) to WD J1330+6435, but exhibited an excess of flux between 4600 and 5100 Å not seen in the B. C. Kaiser et al. (2021) data or model, indicating our model could not be used reliably, and so is not shown here. Extracting the model from their fig. 1, we instead found a sandy yellow colour (#FFEAAB) more appropriate to its low $T_{\rm eff}$.

The DZ white dwarf with a spectrum most severely departing from a blackbody is WD J2356−2054 which was first properly analysed by S. Blouin et al. (2019a). This star was originally discovered by B. R. Oppenheimer et al. (2001), with its spectrum initially described as 'bizarre' due to ultrabroad Na I absorption spanning a large proportion of the optical. The analysis of S. Blouin et al. (2019a) showed that this object could be accurately modelled after recently developed unified profiles of Na-He were included. The spectrum also contains a molecular band from MgH blended with a quasi-molecular satellite of Na-He. We calculated a model with identical parameters to S. Blouin et al. (2019a) which well reproduces their model. The extreme Na absorption is found to practically wipe out visible emission in the centre of the optical, with the perceived colour primarily being weighted to fluxes in the 450–500 nm range. This results in a vivid blue appearance (Fig. B7), despite having a $T_{\rm eff} \simeq 4000$ K. In the chromaticity diagram (Fig. 8), WD J2356−2054 is found to be bluer than even a pure Rayleigh–Jeans tail meaning this low $T_{\rm eff}$ star cannot be assigned a colour temperature.

While WD J2356−2054 appears in a very different part of the chromaticity diagram, it is qualitatively similar to WD J1330+6435 in that they are both cool ($T_{\rm eff} \simeq 4000$ K) white dwarfs with helium dominated atmospheres, and with Na I being the dominant spectral feature (also with prominent absorption from Ca I at 4227 Å). Therefore WD J2356−2054 essentially represents a more extreme version of WD J1330+6435 where, given a large enough sample of cool DZ white dwarfs, a continuum of objects likely exists between them allowing for other DZs with vivid green, cyan, and blue hues which may be identified in future surveys.

3.5 The 20 pc local sample

We conclude Section 3 by examining the chromaticities of all white dwarfs within 20 pc of the Sun. This unbiased volume-limited sample contains 152 white dwarfs[7] (M. A. Hollands et al. 2018b; M. W. O'Brien et al. 2026b) spanning a wide range of $T_{\rm eff}$ and spectroscopic sub-types, and is of sufficient size to probe the statistical properties of white dwarf chromaticities in general. To calculate chromaticities for each of the white dwarfs in the 20 pc volume, we used a mixture of methodologies and sources of parameters depending on the spectral types, with the results listed in Table C6.

The majority of white dwarfs within 20 pc have spectral types DA, DB, or DC. For objects with these classifications we used pure hydrogen and pure helium model grids spanning the same $T_{\rm eff}$ ranges as in Section 3.1, but instead of using a fixed $\log g$ of 8, we used extended grids spanning $\log g$ of 7.0 to 9.0 in steps of 0.5 dex. In practice we found that their chromaticities were almost entirely insensitive to $\log g$. For DCs where the atmospheric composition may be ambiguous, we used the hydrogen/helium compositions of M. W. O'Brien et al. (2024), which is our primary reference for 20 pc white dwarf parameters.

For the 20 pc DQs we once again opted to use optical spectra rather than models, which was particularly necessary for DQpec stars with distorted Swan Bands. Since continuous spectral coverage over the entire visual range, and accurate flux calibration is a necessity for converting spectroscopic data to chromaticities, for most DQs we used spectral data hosted by the Montreal White Dwarf Database (MWDD; P. Dufour et al. 2017) except where noted in Table C6. We applied a similar adjustment to the flux calibrations using PanSTARRS data to that described in Section 3.3.

For DZs within 20 pc, we calculated spectral models using the Koester white dwarf atmospheric model code, adopting atmospheric parameters from the accompanying references in Table C6. Note that for DAZs, the metal lines are sufficiently narrow that they have a negligible effect on the calculated chromaticities, and so we simply used DA models as above in those cases.

The chromaticities for all white dwarfs within 20 pc are shown in the top panel of Fig. 9. The majority of the 20 pc white dwarfs have colours close to the blackbody locus, including most of the DZs and DQs. Only a few extreme stars deviate significantly away from blackbody colours. For objects close to the blackbody locus it is simpler to examine the 1D distribution in terms of correlated colour temperature. We calculated these colour temperatures by converting the CIE 1931 x–y chromaticities for each object to UCS 1960 u–v chromaticities using equation (3), then minimizing the Euclidean distance to the blackbody locus in the u–v plane to find the correlated colour temperature. For non-blackbody colours, e.g. green and magenta, it is not meaningful to assign a colour temperature, and so we excluded objects with distances greater than 0.01 (in u–v terms) from the Planckian-locus. The five rejected objects consisted of two DZs (WD J0842−1347 and WD J2253−0646) both exhibiting yellow hues, and three DQpec white dwarfs (WD J1011+2845, WD J1038−2040, and WD J2157−5100) all with pink colours. From this volume-limited sample, we therefore conclude that only $3.4^{+1.7}_{-1.3}$ percent of white

[7]We do not include the purported cool, nearby white dwarf with *Gaia* DR3 ID 6013647666939138688 found by A. Golovin et al. (2024), as its astrometry appears contaminated, suggesting its large parallax may be erroneous.

Downloaded from academic.oup.com/rasti/article/doi/10.1093/rasti/rzag069/8914458 by guest on 26 October 2026

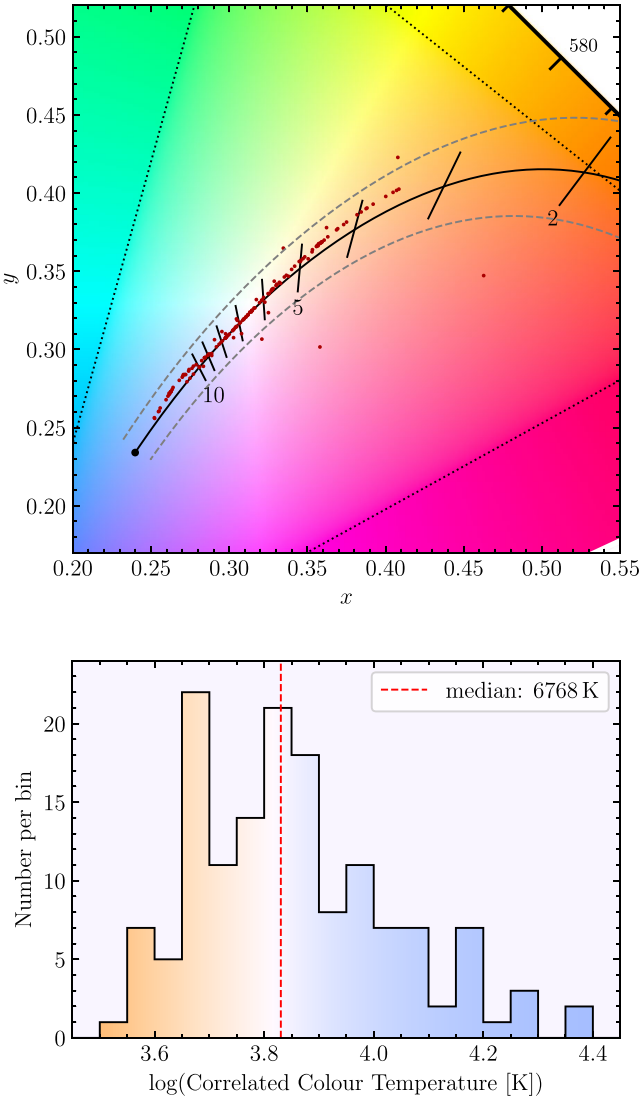

Figure 9. Chromaticity distribution (top) for all white dwarfs within 20 pc of the Sun (points). Our cuts to exclude objects with non-blackbody colours is shown by the grey dashed lines. The correlated colour temperature distribution for the 20 pc sample (excluding three outliers) is shown in the bottom panel, where the colour gradient under the histogram represents the sRGB colour at each given colour temperature, and the panel background is filled with the colour corresponding to the median (#F9F5FF).

dwarfs have chromaticities deviating from blackbodies by more than the above threshold, highlighting the rarity of the more unusual objects we identified in earlier sections.

The correlated colour temperature distribution of the remaining 147 objects are shown in the bottom panel of Fig. 9, demonstrating a range in colour temperatures spanning 3000 to 25 000 K. The median of this distribution, indicated by the vertical dashed line, is located at 6768 K with a corresponding sRGB hex code of #F9F5FF. Evidently this median colour is remarkably close to the D65 white point (a colour temperature of 6504 K), and so (to our amusement) the common depiction of blue tinted white dwarfs is unrepresentative: on average white dwarfs are in fact white, and are therefore appropriately named. Of course this neglects the breadth of the distribution, where we find 95 per cent of objects are contained within the range 3800 to 18 700 K, i.e. a factor of 5 in colour temperature.

4 VISUALIZATION OF WHITE DWARFS

So far, all computed colours have been for observed spectra or disc-integrated models only. The same techniques described in Section 2 can also be applied to spectral models to generate realistic images of stars as they would appear to a nearby observer (though limited in brightness as before), allowing the creation of images that can be used in an outreach setting.

The radiation emitted from the surface of a star is not only a function of wavelength, λ, but also depends on the angle between the surface-normal and the viewing direction, θ. Therefore the fluxes F can be expressed as $F(\lambda, \mu)$ (the spectral radiance) where $\mu = \cos(\theta)$, resulting in limb-darkening of stars, and is an important consideration in the analysis of eclipsing binaries and exoplanet transits (e.g. J.

Downloaded from academic.oup.com/rasti/article/doi/10.1093/rasti/rzag069/8914458 by guest on 26 October 2026

Southworth 2012). Limb-darkening must also be considered to generate accurate images of stars, though not only its effect on brightness across the stellar disc, but also its effect on chromaticity.

Using model atmospheres, the relative flux in various pass-bands can be determined for different values of μ. This is achieved by integrating $F(\lambda, \mu)$ over a passband transmission curve, resulting in a function of μ only, $I(\mu)$. These $I(\mu)$ are then typically fitted with a variety of limb-darkening laws, with the fitted parameters tabulated for all relevant bands and atmospheric parameters (e.g. A. Gianninas et al. 2013; A. Claret et al. 2020). The simplest limb-darkening law, the linear law,

$$\frac{I(\mu)}{I(1)} = 1 - a(1-\mu), \tag{8}$$

contains a single free parameter, a. However, in most cases, $I(\mu)$ departs from a linear dependence on μ and so more complex limb-darkening laws are required for accurate modelling. For instance, the quadratic limb-darkening law extends the linear law by including a $(1-\mu)^2$ term with one further free parameter. The Claret four-term law (A. Claret 2000),

$$\frac{I(\mu)}{I(1)} = 1 - \sum_{k=1}^{4} a_k \left(1 - \mu^{k/2}\right), \tag{9}$$

provides a flexible function for modelling limb-darkening across a wide range of $T_{\rm eff}$ and spectral types, and is the limb-darkening law we use here.

The Koester white dwarf model atmospheres internally calculate the spectral radiance, $F(\lambda, \mu)$, at nine discrete values of μ, which can be output from the spectral synthesis allowing limb-darkening laws to be applied. For a given spectral model, we calculated the XYZ values for each value of μ by integrating over $F(\lambda, \mu)$ using equation (1). As before we then converted these to linear sRGB using equation (4), with each channel now a function of μ. We then fitted limb-darkening laws to each of the R, G, and B channels, by minimizing the squared differences between the limb-darkening model and the RGB channel values. In our testing, only the Claret four-term law could reliably fit all RGB curves without leaving excessive residuals. Finally we rescaled the best-fitting limb-darkening curves so that brightest RGB value had an intensity of 1 at $\mu = 1$, maintaining the relative intensities between the R, G, and B, thereby allowing linear sRGB values to be evaluated at any point on the stellar disc.

We used our fitted and scaled limb darkening curves to generate images within the unit circle, interpolating the fitted sRGB limb-darkening curves for each pixel in the images. These images were then converted to display sRGB by applying gamma-correction using equation (7). Note that the inclusion of gamma-correction is especially important here, as its omission leads not only to incorrect chromaticities but also greatly exaggerated limb-darkening.

We generated images for a small sample of DAs, DQs, and DZs which are shown in the right panels of Figs B8–B11. These are accompanied by a selection of panels showing the spectra (top left), with the bottom left panels demonstrating the fitted limb-darkening curves in terms of sRGB intensity versus μ, sRGB intensity versus r (where $r^2 = 1 - \mu^2$), and chromaticity versus r, from left to right.

For the DAs, we generated three models at $T_{\rm eff} = 7000$, 10 000, and 20 000 K, all at $\log g = 8$. While the linear intensities decrease by up to 80 per cent (in the 7000 K model) from the centre to the limb, the change in perceived intensity in the final images is fairly minor, due to the non-linear response of the human visual system (Section 2.3), and because most of the change occurs rapidly in the outermost pixels only. As a result, the three DA images appear as almost flat discs. The chromaticity as a function of r panels demonstrate that this quantity is almost constant across the entire stellar disc with small changes seen at the very limbs. This results in a slightly less intense shade of blue at the very edges of the stellar discs, where the RGB intensities are close to equal near $\mu = 0$ for the 7000 and 10 000 K models.

In Sections 3.3 and 3.5 we restricted ourselves to observed DQ spectra, in order to determine accurate chromaticities. However, to generate images of these carbon-rich stars, it is necessary to use angular-dependent model spectra. Using the Koester white dwarf model atmosphere code, we have generated models for three DQs with increasingly complex Swan band features, WD J0136+2004, WD J0902+2010, and WD J1011+2845. The greatest challenge in modelling these stars is capturing the distortion of the C_2 Swan bands. Kowalski (2010) demonstrated that this occurs due to shifts in their electronic transition energy, ΔT_e, that is proportional to the atmospheric density, ρ, i.e. $\Delta T_e = \alpha\rho$, where ΔT_e is in eV, and ρ is in g cm^{-3}. Using density functional theory methods Kowalski (2010) found a value of $\alpha = 1.6$, though this severely overestimates the observed level of distortion. Instead S. Blouin et al. (2019b) determined an empirical value of $\alpha = 0.2$, which was found to produce acceptable results for many peculiar DQs, though still failed in some extreme cases. Studying the evolution of DQ stars S. Blouin & P. Dufour (2019) found that carbon-rich white dwarfs transition from DQs to DQpec when their photospheric densities reach 0.15 g cm^{-3}. We adopted the $\alpha = 0.2$ calibrated by S. Blouin et al. (2019b) in our models. For WD J0136+2004 we adopted parameters from S. Coutu et al. (2019), for WD J0902+2010 we used parameters found by S. Blouin & P. Dufour (2019), and for WD J1011+2845 we used S. Blouin et al. (2019b) parameters.

Our DQ images are shown in Fig. B9. In all three cases, limb darkening is now readily apparent compared to the DAs, due to their atmospheres being primarily composed of dense helium. WD J0136+4513 appears a pale lilac colour in the centre of the disc, with a chromaticity shifting towards fainter and more pink hues at the limb of the star. The image for the DQpec WD J0902+2010 is pink throughout, though the colour becomes less vivid towards the limb. Despite some minor differences between the model and SDSS spectrum (the ridges between the Swan bands are slightly more pronounced in the model), the overall colour is fairly similar to that found in Fig. B4. Finally we show the reddish-pink DQpec WD J1011+2845. Like S. Blouin et al. (2019b), our model does not fully

Downloaded from academic.oup.com/rasti/article/doi/10.1093/rasti/rzag069/8914458 by guest on 26 October 2026

reproduce the roundness of the Swan bands, which are much more distorted in the data (Fig. B4), possibly due to the presence of a magnetic field (G. D. Schmidt et al. 1999). Overall this results in an disc-averaged model colour (#FF7A65) which is more vivid than the observed spectrum (#FF8775), though the model still retains the salmon pink hue found from the data. Like the other DQs the limb-darkening is quite pronounced, and also shows a shift to a less vivid tone towards the disc edge.

For the DZs we generated images for six objects in order to demonstrate the wider range of chromaticities for these stars, which are shown in Figs B10 and B11. The first of these WD J1535+1247 has a typical cool DZ spectrum, and is a well studied (D. Koester et al. 2011; M. A. Hollands et al. 2017; S. Blouin et al. 2019b; S. Coutu et al. 2019; M. A. Hollands et al. 2022) member of the 20 pc sample (M. A. Hollands et al. 2018b). Owing to its near-Solar $T_{\rm eff}$ the centre of the disc is close in colour to the D65 white point, i.e. all three RGB values are close to 1 for $\mu = 1$. However, limb-darkening induces a golden hue around the edge of the star. WD J0916+2540, first analysed by D. Koester et al. (2011) has a complex spectrum resulting from large metal abundances, giving it a pale yellow-orange colour. While limb-darkening in its image is apparent, the chromaticity shift is more subtle for this object. WD J0744+4649 is a similar case, with its vivid yellow colour remaining near constant in chromaticity across the disc, where the R and G values are near equal over all values of μ.

We show two green objects in Fig. B11. The first of these, WD J0851+1543 is relatively pale, but shows a complex change in chromaticity across the disc. At the disc centre, the G and B values are virtually identical (pale cyan), but becomes G dominated for $\mu < 0.9$ ($r > 0.4$). However, for $\mu < 0.15$ ($r > 0.99$), R becomes the dominant channel, giving a slight yellow hue to the very limb of WD J0851+1543. WD J1330+6435 exhibits a more vivid green colour (#D0FFB4) at the disc centre, though the colour becomes less saturated towards the limbs before becoming R dominated for $\mu < 0.2$ ($r > 0.98$). Upon close inspection of the image, this gives WD J1330+6435 an orange hue in the outermost pixels of its disc. Finally, we show WD J2356−2054, which (as discussed in Section 3.4) is essentially a more metal-rich analogue of WD J1330+6435 with an even larger sodium abundance. Despite being only 4000 K, the star is a vivid blue across its entire disc. Unlike the DA models shown in Fig. B8, which are blue due to their high $T_{\rm eff}$, WD J2356−2054 shows strong limb darkening, betraying the nature of its cool helium-dominated atmosphere.

Images such as those shown in Figs B8–B11 show that the appearances of white dwarfs are highly diverse. This is shown to be particularly true for cool white dwarfs with helium dominated-atmospheres enriched in heavy elements where the strong opacity sources results in not only unusual colours, but also chromaticity shifts across the stellar disc due to limb darkening.

5 CONCLUSIONS

We have shown that white dwarfs exhibit a wide range of chromaticities. We found that the chemically simplest white dwarfs with pure hydrogen or helium atmospheres closely follow the blackbody locus in the chromaticity diagram. In volume-limited samples, we established that white dwarfs have a median correlated colour temperature of 6800 K, and so on average white dwarfs are indeed white in colour, rather than the canonical blue hue corresponding to hot white dwarfs which are over-represented in magnitude-limited samples.

More exotic white dwarfs, i.e. those with carbon or other metals in their atmospheres, may exhibit extremely broad absorption features at optical wavelengths. For DQs we found this results in pink and purple stars, whereas for DZs we identified examples known objects with yellow and green hues. Furthermore, IR faint white dwarfs with mixed hydrogen/helium atmospheres turn towards cyan colours due to collision induced absorption of H_2-He encroaching into optical wavelengths.

Finally, we demonstrated that calculations typically used to determine limb-darkening coefficients from model atmospheres can be applied to generate realistic images of stars. In the case of DQ and DZ white dwarfs, the dramatic limb-darkening can lead to strong variations in both perceived intensity and chromaticity across the stellar disc. We expect such images to be useful in an outreach setting, highlighting the non-blackbody radiation emitted from stellar atmospheres under extreme physical conditions.

ACKNOWLEDGEMENTS

The authors thank the referee, Patrick Dufour, for their constructive feedback. MAH acknowledges a Warwick Astrophysics prize post-doctoral fellowship made possible thanks to a generous philanthropic donation. PET and BTG received funding from the European Research Council under the European Union's Horizon 2020 research and innovation programme number 101002408 (MOS100PC) and 101020057 (WDPLANETS). DK acknowledges V. Alekseev for Na-He adiabatic potentials and dipole moments used for Na unified profiles. MAH acknowledges M. W. O'Brien for the use of DZ models from the 13 pc sample, A. Stockman for useful conversations about colour matching functions, and J. J. Hermes, R. P. Ashley, and C. E. Pugh for continued encouragement to publish this unconventional analysis.

CONFLICTS OF INTEREST

The authors declare no conflict of interest.

DATA AVAILABILITY

All observed spectra were obtained from publicly available SDSS data or from the Montreal White Dwarf Database. Spectral models for individual objects are available upon reasonable request.

Downloaded from academic.oup.com/rasti/article/doi/10.1093/rasti/rzag069/8914458 by guest on 26 October 2026

REFERENCES

Alam S. et al., 2015, ApJS, 219, 12
Allard N. F., Alekseev V. A., 2014, Adv. Space Res., 54, 1248
Allard N., Kielkopf J., 1982, Rev. Mod. Phys., 54, 1103
Allard N. F., Royer A., Kielkopf J. F., Feautrier N., 1999, Phys. Rev. A, 60, 1021
Allard N. F., Kielkopf J. F., Allard F., 2007, Eur. Phys. J. D, 44, 507
Allard N. F., Guillon G., Alekseev V. A., Kielkopf J. F., 2016a, A&A, 593, A13
Allard N. F., Leininger T., Gadéa F. X., Brousseau-Couture V., Dufour P., 2016b, A&A, 588, A142
Allard N. F. et al., 2020, MNRAS, 494, 868
Bergeron P., Leggett S. K., 2002, ApJ, 580, 1070
Bergeron P., Ruiz M. T., Leggett S. K., 1997, ApJS, 108, 339
Bergeron P., Kilic M., Blouin S., Bédard A., Leggett S. K., Brown W. R., 2022, ApJ, 934, 36
Bernath P. F., 2009, Int. Rev. Phys. Chem., 28, 681
Blanton M. R. et al., 2017, AJ, 154, 28
Blouin S., Dufour P., 2019, MNRAS, 490, 4166
Blouin S., Kowalski P. M., Dufour P., 2017, ApJ, 848, 36
Blouin S., Dufour P., Allard N. F., 2018, ApJ, 863, 184
Blouin S., Dufour P., Allard N. F., Salim S., Rich R. M., Koopmans L. V. E., 2019a, ApJ, 872, 188
Blouin S., Dufour P., Thibeault C., Allard N. F., 2019b, ApJ, 878, 63
Blouin S., Kilic M., Albert L., Azartash-Namin B., Dufour P., 2024, ApJ, 976, 218
Borysow A., Jorgensen U. G., Fu Y., 2001, J. Quant. Spectrosc. Radiat. Transfer, 68, 235
Bues I., 1999, in Solheim J. E., Meistas E. G., eds, ASP Conf. Ser. Vol. 169, 11th European Workshop on White Dwarfs. Astron. Soc. Pac., San Francisco, p. 240
Burrows A., 2001, in Ultracool Dwarfs: New Spectral Types L and T. Springer, Berlin, p. 26
Burrows A., Sudarsky D., Lunine J. I., 2003, ApJ, 596, 587
Cardiel N. et al., 2021, MNRAS, 504, 3730
Caron A., Bergeron P., Blouin S., Leggett S. K., 2023, MNRAS, 519, 4529
Technical Note, 1960, J. Opt. Soc. Am., 50, 89
Claret A., 2000, A&A, 363, 1081
Claret A., Cukanovaite E., Burdge K., Tremblay P. E., Parsons S., Marsh T. R., 2020, A&A, 641, A157
Coutu S., Dufour P., Bergeron P., Blouin S., Loranger E., Allard N. F., Dunlap B. H., 2019, ApJ, 885, 74
Cranmer S. R., 2021, Res. Notes Am. Astron. Soc., 5, 201
Cukanovaite E., Tremblay P. E., Freytag B., Ludwig H. G., Bergeron P., 2018, MNRAS, 481, 1522
Cukanovaite E., Tremblay P. E., Freytag B., Ludwig H. G., Fontaine G., Brassard P., Toloza O., Koester D., 2019, MNRAS, 490, 1010
Cukanovaite E., Tremblay P.-E., Bergeron P., Freytag B., Ludwig H.-G., Steffen M., 2021, MNRAS, 501, 5274
Dawson K. S. et al., 2013, AJ, 145, 10
Dufour P., Liebert J., Fontaine G., Behara N., 2007, Nature, 450, 522
Dufour P., Blouin S., Coutu S., Fortin-Archambault M., Thibeault C., Bergeron P., Fontaine G., 2017, in Tremblay P.-E., Gänsicke B., Bergeron P., eds, ASP Conf. Ser. Vol. 509, 20th European White Dwarf Workshop. Astron. Soc. Pac., San Francisco, p. 3
Elms A. K., Tremblay P.-E., Gänsicke B. T., Koester D., Hollands M. A., Gentile Fusillo N. P., Cunningham T., Apps K., 2022, MNRAS, 517, 4557
Evans T. M. et al., 2013, ApJ., 772, L16
Farihi J., Bond H. E., Dufour P., Haghighipour N., Schaefer G. H., Holberg J. B., Barstow M. A., Burleigh M. R., 2013, MNRAS, 430, 652
Foley J., van Dam A., Feiner S., Hughes J., 1982, Computer Graphics: Principles and Practice, 2nd edn. Addison Wesley, Boston
Fong J. et al., 2025, Sci. Adv., 11, eadu1052
Fontaine G., Villeneuve B., Wesemael F., Wegner G., 1984, ApJ, 277, L61
Gänsicke B. T., Koester D., Farihi J., Toloza O., 2018, MNRAS, 481, 4323
Gao P., Wakeford H. R., Moran S. E., Parmentier V., 2021, J. Geophys. Res. (Planets), 126, e06655
Giammichele N., Bergeron P., Dufour P., 2012, ApJS, 199, 29
Gianninas A., Strickland B. D., Kilic M., Bergeron P., 2013, ApJ, 766, 3
Golovin A., Reffert S., Vani A., Bastian U., Jordan S., Just A., 2024, A&A, 683, A33
Hall R., 1988, Illumination and Color in Computer Generated Imagery. Springer, New York
Hall P. B., Maxwell A. J., 2008, ApJ, 678, 1292
Harre J.-V., Heller R., 2021, Astron. Nachr., 342, 578
Harrison J. H. D., Bonsor A., Kama M., Buchan A. M., Blouin S., Koester D., 2021, MNRAS, 504, 2853
Hauschildt P. H., Allard F., Baron E., 1999, ApJ, 512, 377
Hollands M. A., Koester D., Alekseev V., Herbert E. L., Gänsicke B. T., 2017, MNRAS, 467, 4970
Hollands M. A., Gänsicke B. T., Koester D., 2018a, MNRAS, 477, 93
Hollands M. A., Tremblay P.-E., Gänsicke B. T., Gentile-Fusillo N. P., Toonen S., 2018b, MNRAS, 480, 3942
Hollands M. A., Tremblay P.-E., Gänsicke B. T., Koester D., Gentile-Fusillo N. P., 2021, Nat Astron., 5, 451
Hollands M. A., Tremblay P. E., Gänsicke B. T., Koester D., 2022, MNRAS, 511, 71
1999, Multimedia systems and equipment – colour measurement andmanagement – part 2-1: Colour management - default RGB colour space –sRGB, 61966-2-1, International Electrotechnical Comission
Irwin P. G. J. et al., 2024, MNRAS, 527, 11521
Judd D. B., 1951, in In Proceedings of the Twelfth Session of the CIE, Stockholm, Vol. 1. Bureau Central de la CIE, Paris, p. 11
Judd D., Wyszecki G., 1975, Color in Business, Science, and Industry, 3rd edn. Wiley, New York
Jura M., 2003, ApJ, 584, L91
Kaiser B. C., Clemens J. C., Blouin S., Dufour P., Hegedus R. J., Reding J. S., Bédard A., 2021, Science, 371, 168

Downloaded from academic.oup.com/rasti/article/doi/10.1093/rasti/rzag069/8914458 by guest on 26 October 2026

Kawka A., Vennes S., Allard N. F., Leininger T., Gadéa F. X., 2021, MNRAS, 500, 2732
Kepler S. O. et al., 2016, MNRAS, 455, 3413
Koester D., 2010, Mem. Soc. Astron. Ital., 81, 921
Koester D., Weidemann V., Zeidler E.-M., 1982, A&A, 116, 147
Koester D., Girven J., Gänsicke B. T., Dufour P., 2011, A&A, 530, A114
Kohman T. P., 2005, J. R. Astron. Soc. Can., 99, 98
Kowalski P. M., 2010, A&A, 519, L8
Kowalski P. M., 2014, A&A, 566, L8
Kowalski P. M., Saumon D., 2006, ApJ, 651, L137
Luyten W. J., 1922, PASP, 34, 54
MacAdam D. L., 1937, J. Opt. Soc. Am., 27, 294
MacLeod D. et al., 2006, Fundamental chromaticity diagram with physiological axes–part 1, Tech. Rep. 170-1, International Comission on Illumination.
Murdin P., 1981, Quart. J. R. Astron. Soc., 22, 353
Murdin P., 1987, J. Brit. Astron. Assoc., 97, 204
O'Brien M. W. et al., 2024, MNRAS, 527, 8687
O'Brien M. W. et al., 2026a, MNRAS, 552, stag1669
O'Brien M. W., Wilson D. J., Tremblay P.-E., Gänsicke B. T., Byrne C. M., Lagos-Vilches F., Pineda J. S., Barraza-Jorquera J. A., 2026b, MNRAS, 550, stag1195
Oppenheimer B. R., Hambly N. C., Digby A. P., Hodgkin S. T., Saumon D., 2001, Science, 292, 698
Rering O., Charnay B., 2025, Res Notes Am. Astron. Soc., 9, 168
Rohrmann R. D., Althaus L. G., Kepler S. O., 2011, MNRAS, 411, 781
Sahu S. et al., 2025, MNRAS, 543, 223
Saumon D., Blouin S., Tremblay P.-E., 2022, Phys. Rep., 988, 1
Savino M., Comins N. F., 2015, in American Astronomical Society Meeting Abstracts #225. p. 422.05
Schmidt G. D., Bergeron P., Fegley B., 1995, ApJ, 443, 274
Schmidt G. D., Liebert J., Harris H. C., Dahn C. C., Leggett S. K., 1999, ApJ, 512, 916
Schmidt G. D. et al., 2003, ApJ, 595, 1101
Serenelli A., Rohrmann R. D., Fukugita M., 2019, A&A, 623, A177
Sion E. M., Greenstein J. L., Landstreet J. D., Liebert J., Shipman H. L., Wegner G. A., 1983, ApJ, 269, 253
Smith T., Guild J., 1931, Trans. Opt. Soc., 33, 73
Southworth J., 2012, in Orbital Couples: Pas de Deux in the Solar System and the Milky Way. Observatoire de Paris, Paris, p. 51. Available at: https://sci.esa.int/web/gaia/-/49431-orbital-couples-pas-de-deux-in-the-solar-system-and-the-milky-way
Stockman A., Sharpe L. T., 2000, Vision Res, 40, 1711
Suzuki N., Fukugita M., 2018, AJ, 156, 219
Tootell R. B. H., Nasr S., 2020, Cereb. Cortex, 31, 1163
Tremblay P.-E., Bergeron P., Gianninas A., 2011, ApJ, 730, 128
Tremblay P.-E., Ludwig H.-G., Steffen M., Freytag B., 2013, A&A, 559, A104
Tremblay P.-E. et al., 2017, MNRAS, 465, 2849
Viénot F. et al., 2015, Fundamental chromaticity diagram with physiological axes–part 2: Spectral luminous efficiency functions and chromaticity diagrams, Tech. Rep. 170-2, International Comission on Illumination
Vincent O., Barstow M. A., Jordan S., Mander C., Bergeron P., Dufour P., 2024, A&A, 682, A5
Vos J. J., 1978, Color Res. Appl., 3, 125
Williams J. T., Gänsicke B. T., Swan A., O'Brien M. W., Izquierdo P., Cutolo A.-M., Cunningham T., 2024, A&A, 691, A352
Williams J. T. et al., 2025, MNRAS, 541, 1377
Wyszecki G., Stiles W., 1982, Color science: concepts and methods, quantitative data and formulae, 2nd edn. Wiley, New York, Chichester
Xu S., Zuckerman B., Dufour P., Young E. D., Klein B., Jura M., 2017, ApJ, 836, L7
York D. G. et al., 2000, AJ, 120, 1579
Zuckerman B., Koester D., Melis C., Hansen B. M., Jura M., 2007, ApJ, 671, 872
Zuckerman B., Melis C., Klein B., Koester D., Jura M., 2010, ApJ, 722, 725
Zwinkels J., Sperling A., Goodman T., Campos Acosta J., Ohno Y., Rastello M. L., Stock M., Woolliams E., 2016, Metrologia, 53, G1

APPENDIX A: LUMINANCE

Throughout this work, we have largely ignored the perceived brightness for all objects we have considered, as computer displays are (thankfully) many orders of magnitude fainter than the surfaces of stars. Therefore all displayed colours and images are generated to be as bright as the sRGB standard allows, while still preserving chromaticity. For completeness, we demonstrate here how the perceived brightness can also be calculated from spectral models.

In Section 2, we noted that $\bar{y}(\lambda)$ is equivalent to the photopic luminous efficiency function, i.e. the overall spectral sensitivity of the human eye in photopic conditions. Therefore the integral defining Y (equation 1) can be used to represent brightness. More specifically, Y can be defined as one of several luminous quantities according to a modified version of equation (1) scaled by a prefactor[8]

[8]The luminous efficacy constant defining the candela, $K_{\rm cd}$, is defined to be exactly $683\,{\rm lm\,W^{-1}}$ for a frequency of 540 THz, with a corresponding air wavelength of 555.017 nm. Because the CIE photopic luminous efficiency function, $\bar{y}(\lambda)$, instead peaks at 555 nm exactly, the scaling factor in equation (A1) is slightly higher than $K_{\rm cd}$.

Downloaded from academic.oup.com/rasti/article/doi/10.1093/rasti/rzag069/8914458 by guest on 26 October 2026

(J. Zwinkels et al 2016),

$$Y = 683.002 \frac{\mathrm{lm}}{\mathrm{W}} \int_{360}^{830} F_\lambda(\lambda) \cdot \bar{y}(\lambda)\, \mathrm{d}\lambda, \tag{A1}$$

where λ is again in nm and 1 lm (short for 1 lumen) is the unit of luminous flux. The specific quantity and units of Y therefore depend on the units of F_λ.

If F_λ is the spectral irradiance of an observed star with units $\mathrm{W\,m^{-2}\,nm^{-1}}$ (or more typically $\mathrm{erg\,s^{-1}\,cm^{-2}\,\AA^{-1}}$ in astronomy), then Y is the illuminance, with units of $\mathrm{lm\,m^{-2}}$ (or equivalently lux). For a flat spectrum in F_λ with a *Gaia* apparent magnitude of $G = 10$ (similar to some of the brightest nearby white dwarfs), the illuminance is a mere $Y = 1.85 \times 10^{-10}$ lux. If instead F_λ represents the spectral flux density radiated from the surface of a star (with the same units), then Y represents the luminous exitance, and is again measured in $\mathrm{lm\,m^{-2}}$ (lux is not used). However, if we wish to describe how bright some point appears on the surface of resolved object (independent of its size or distance to the observer), we must consider the directional component of the radiated flux (as in Section 4). Therefore if F_λ is the spectral radiance with units equivalent to $\mathrm{W\,m^{-2}\,sr^{-1}\,nm^{-1}}$, then Y is termed the luminance, with units $\mathrm{lm\,sr^{-1}\,m^{-2}}$. More typically the luminance is expressed in equivalent units[9] of $\mathrm{cd\,m^{-2}}$, where the SI base unit of luminous intensity, the candela (cd), is equivalent to $\mathrm{lm\,sr^{-1}}$.

The calculation of synthetic stellar spectra (such as the Koester white dwarf models) requires the spectral radiance to be calculated at a variety of angles in order to integrate over the stellar disc and compare with observations. We are therefore able to calculate the luminance across the stellar disc for our models shown in Section 4. Using equation (A1), we have calculated the luminance at the centre of the stellar disc for a few of the objects in Appendix Figs B8–B11. The brightest object shown is the 20 000 K DA model with a central luminance of 5.1×10^{10} $\mathrm{cd\,m^{-2}}$, whereas the faintest is WD J2356−2054 at 2.3×10^{8} $\mathrm{cd\,m^{-2}}$. For WD J1535+1247, the central luminance is 2.8×10^{9} $\mathrm{cd\,m^{-2}}$ which is broadly similar to the luminance of the Solar disc without attenuation from the Earth's atmosphere, owing to the similar T_{eff} of this white dwarf to the Sun. In comparison, standard dynamic range computer displays (SDR) have peak luminances of a few 100 $\mathrm{cd\,m^{-2}}$, whereas modern high dynamic range (HDR) displays can reach several 1000 $\mathrm{cd\,m^{-2}}$. Evidently, the brightest computer displays are vastly outshone by even the faintest white dwarfs.

That being said, a luminance of 1000 $\mathrm{cd\,m^{-2}}$ corresponds to an approximately 1330 K blackbody. Therefore for a subset of brown dwarfs, images could be generated with accurate luminances, without scaling to the limits of the display. Of course the optical tails of brown dwarf spectra will appear different to blackbodies (A. Burrows 2001), and so the actual T_{eff}-range without luminance-scaling would require analysis of brown dwarf spectral models which is beyond the scope of this work.

APPENDIX B: ADDITIONAL FIGURES

[9]For display technology the 'nit' is often used as an equivalent unit for the luminance.

Downloaded from academic.oup.com/rasti/article/doi/10.1093/rasti/rzag069/8914458 by guest on 26 October 2026

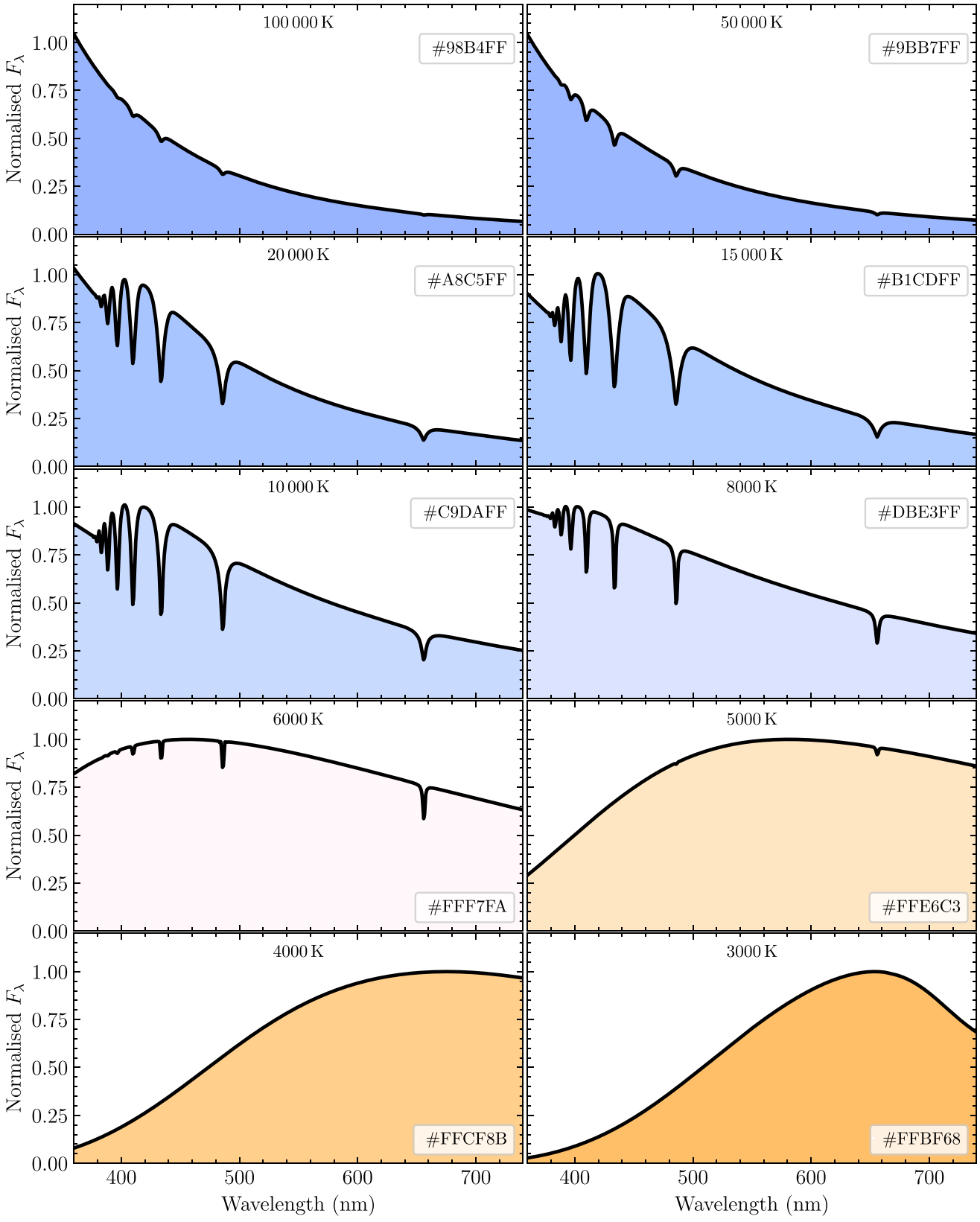

Figure B1. A sample of pure hydrogen (DA) model spectra of different $T_{\rm eff}$. Each spectrum is filled underneath with its calculated sRGB colour with the corresponding sRGB hexcode overplotted on the figure.

Downloaded from academic.oup.com/rasti/article/doi/10.1093/rasti/rzag069/8914458 by guest on 26 October 2026

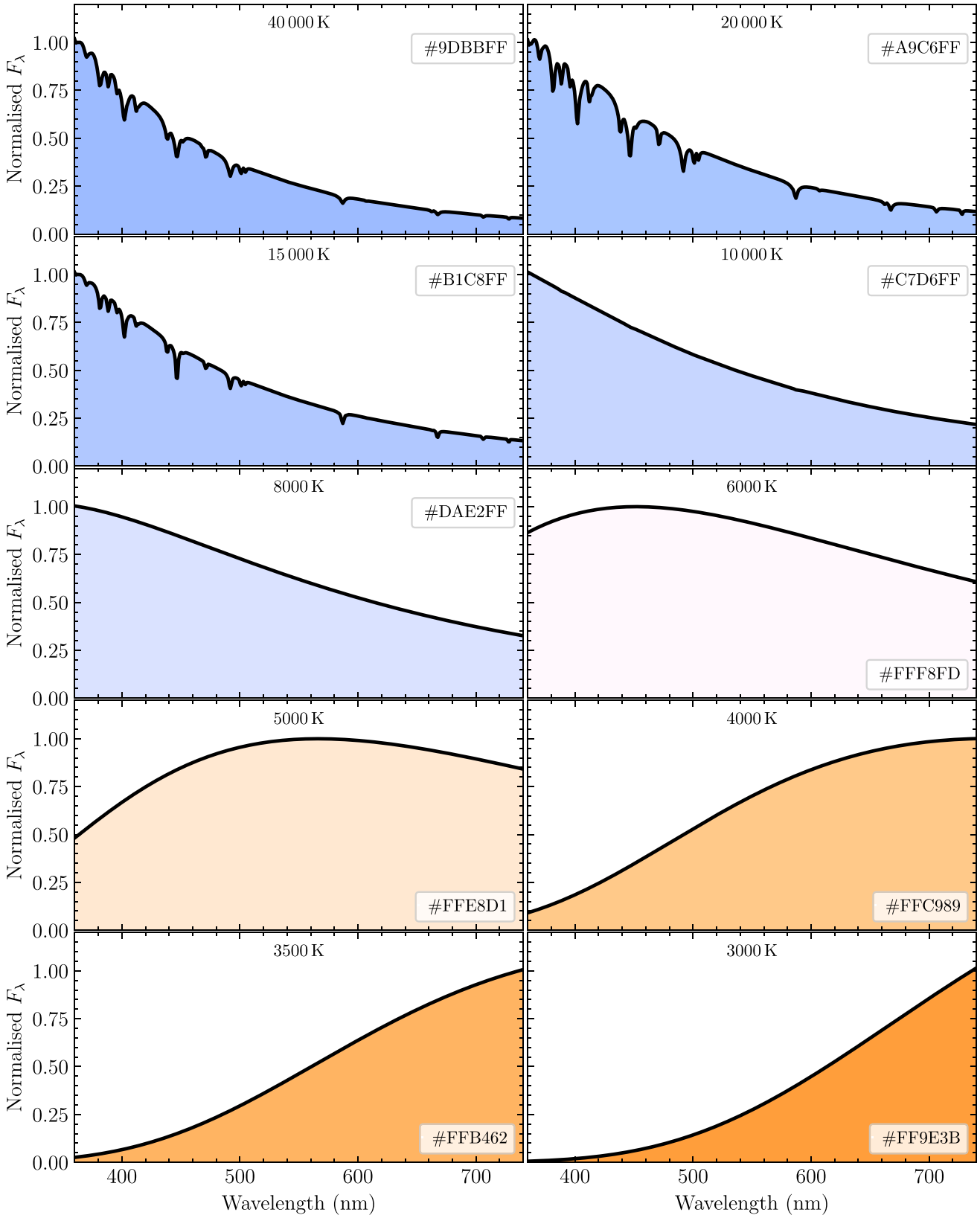

Figure B2. Same as Fig. B1, but for pure helium (DBs) instead.

Downloaded from academic.oup.com/rasti/article/doi/10.1093/rasti/rzag069/8914458 by guest on 26 October 2026

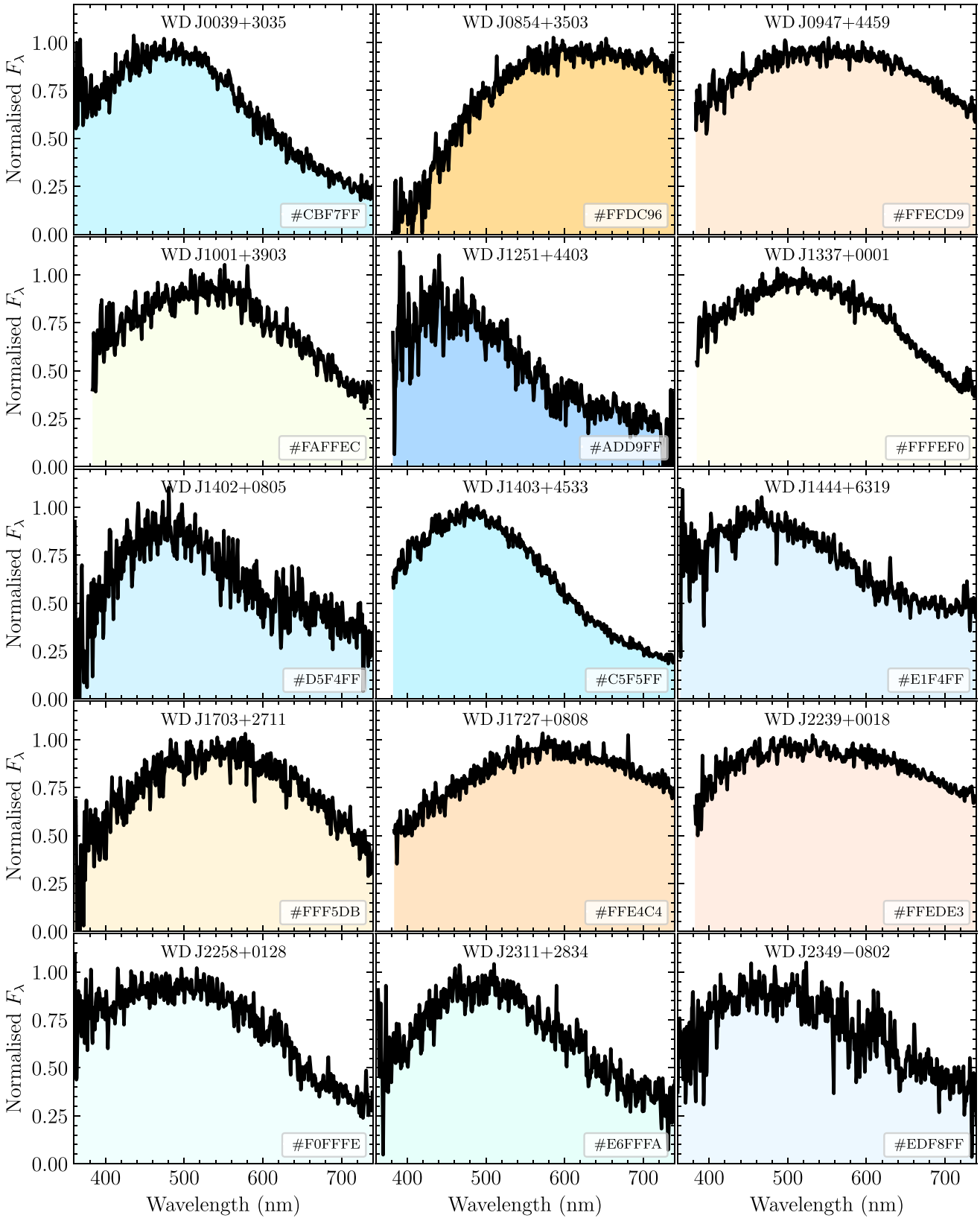

Figure B3. Same as Fig. B1, but for IR-faint white dwarfs instead. Full coordinates are given in Table C3.

Downloaded from academic.oup.com/rasti/article/doi/10.1093/rasti/rzag069/8914458 by guest on 26 October 2026

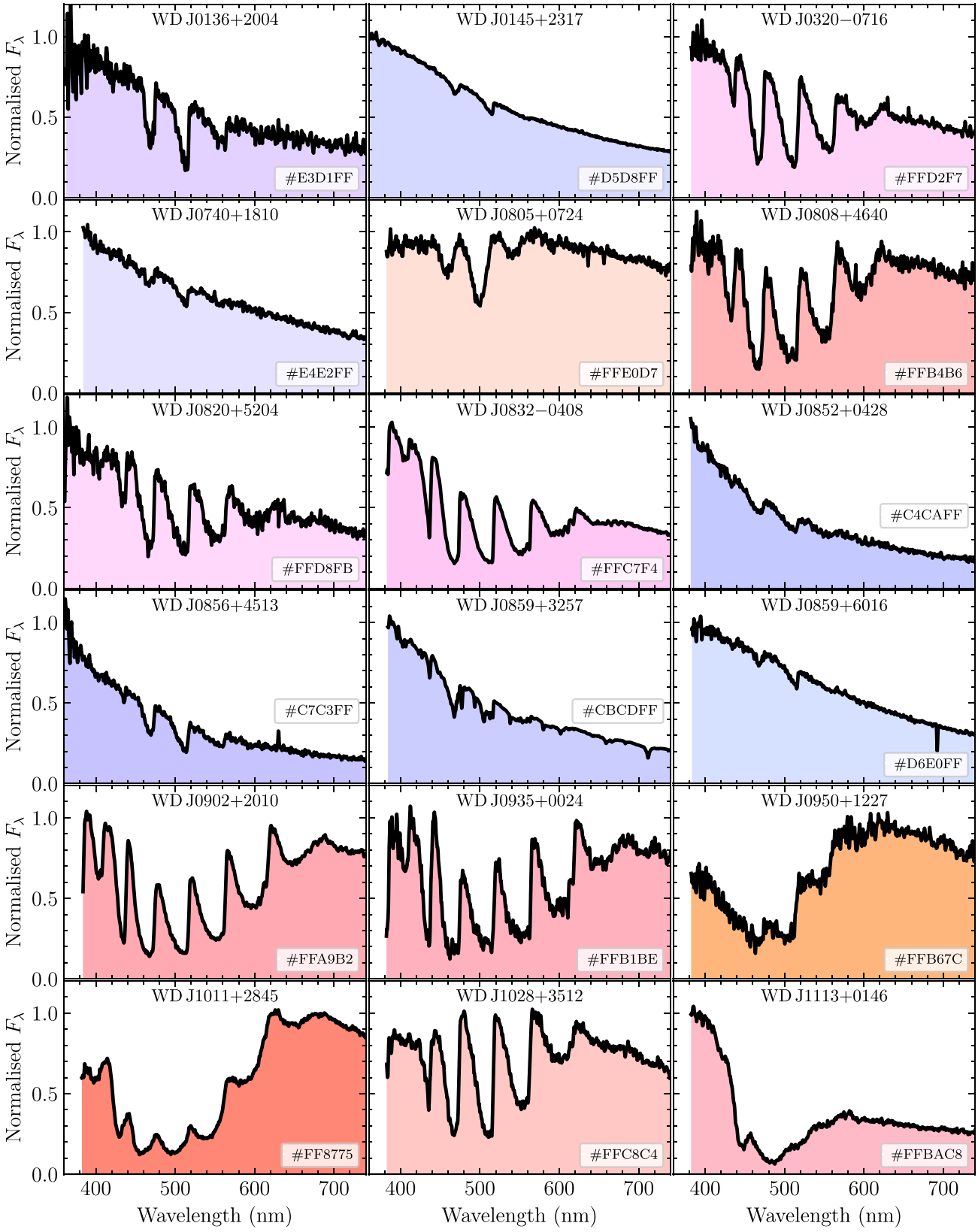

Figure B4. Same as Fig. B1, but for DQs instead. Full coordinates are given in Table C4.

Downloaded from academic.oup.com/rasti/article/doi/10.1093/rasti/rzag069/8914458 by guest on 26 October 2026

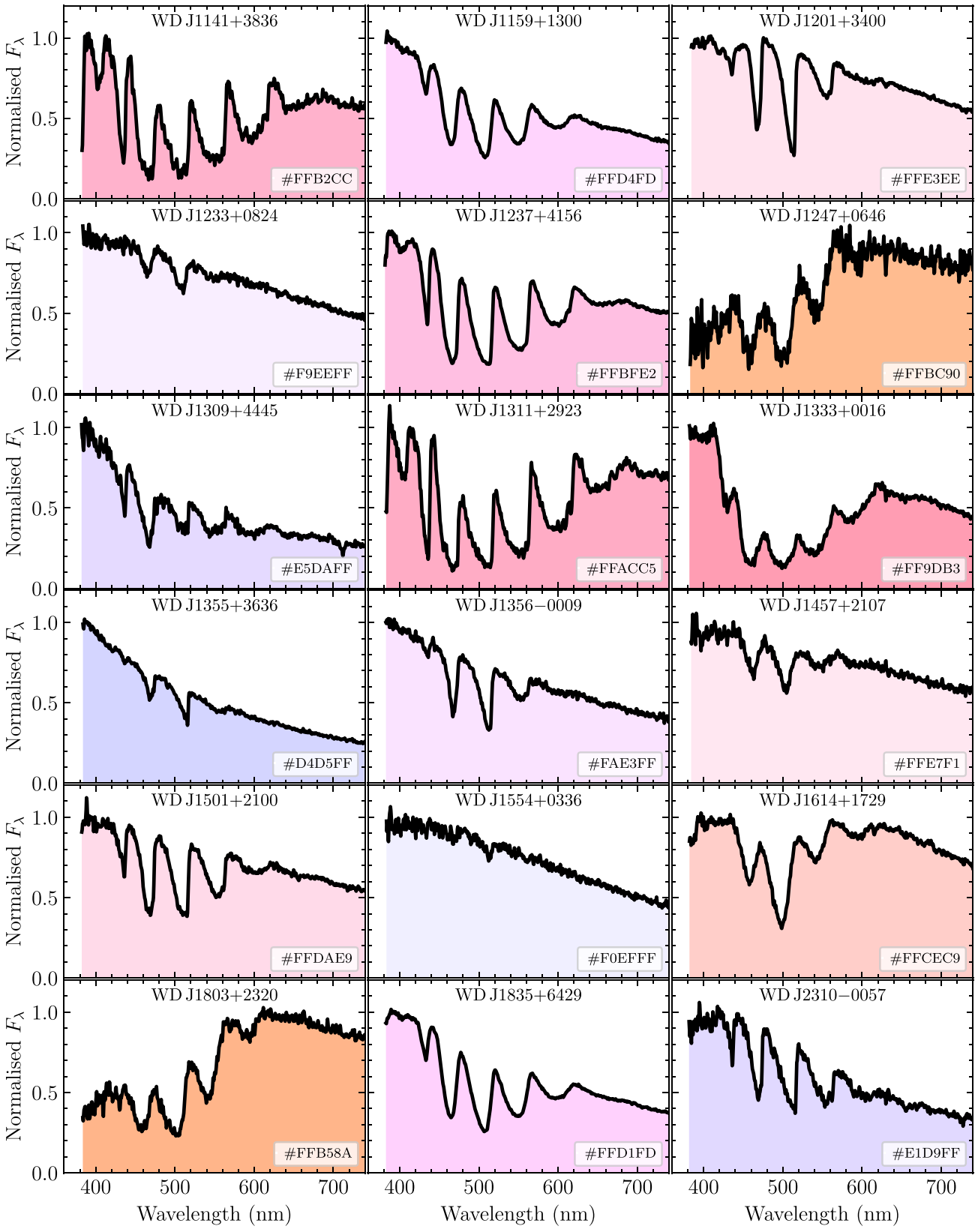

Figure B5. Additional DQ spectra.

Downloaded from academic.oup.com/rasti/article/doi/10.1093/rasti/rzag069/8914458 by guest on 26 October 2026

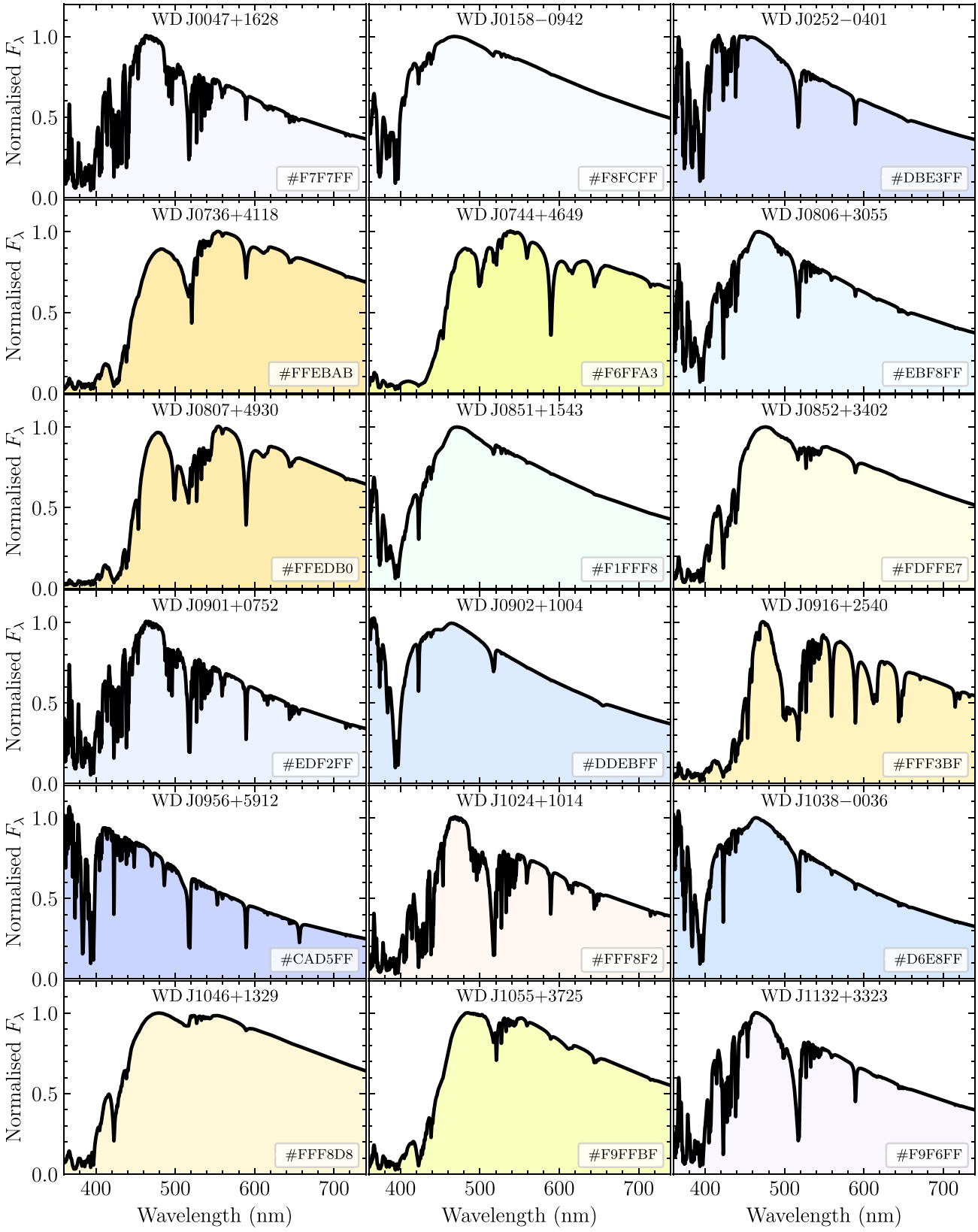

Figure B6. Same as Fig. B1, but for DZs instead. Full coordinates are given in Table C5.

Downloaded from academic.oup.com/rasti/article/doi/10.1093/rasti/rzag069/8914458 by guest on 26 October 2026

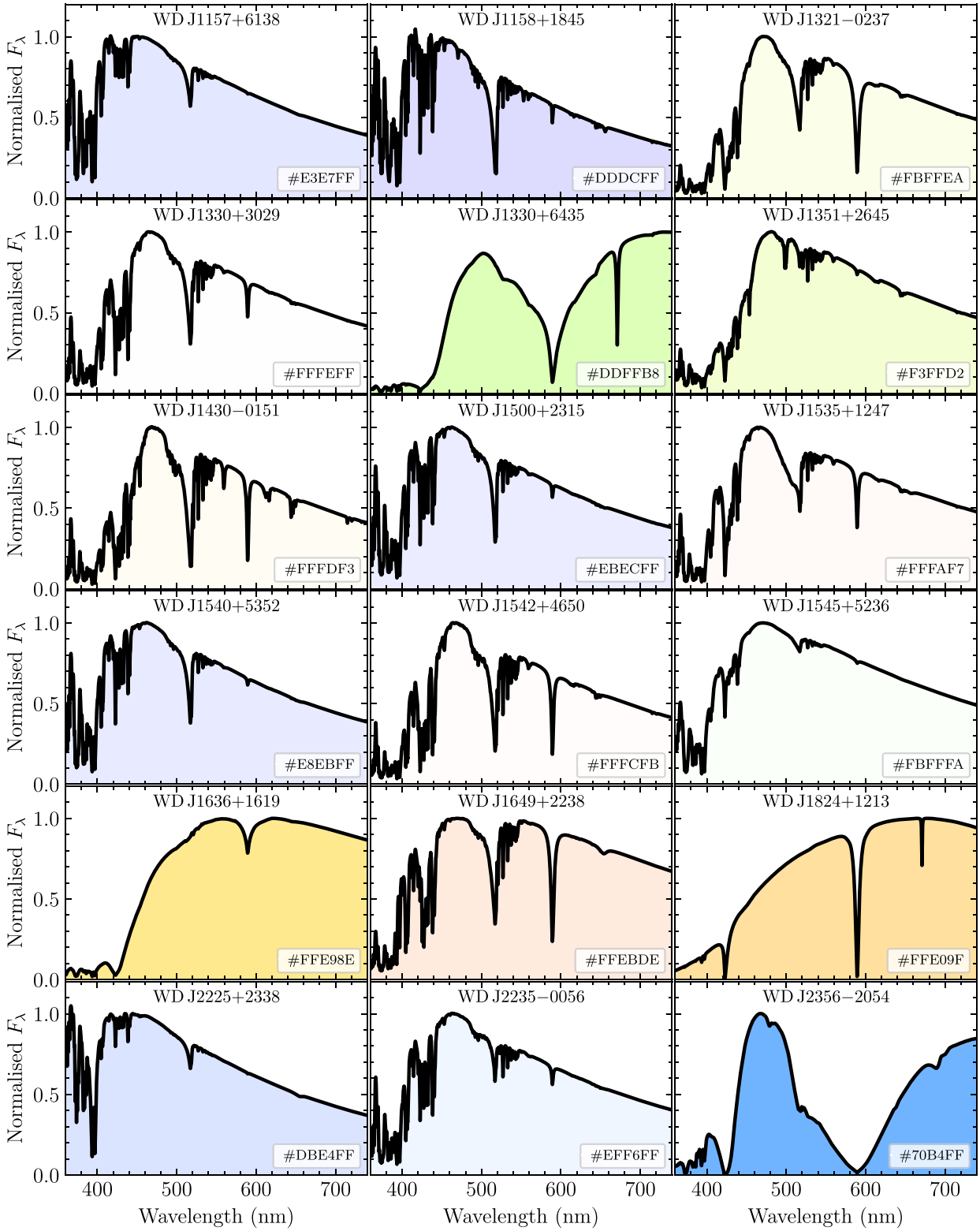

Figure B7. Additional DZ spectra.

Downloaded from academic.oup.com/rasti/article/doi/10.1093/rasti/rzag069/8914458 by guest on 26 October 2026

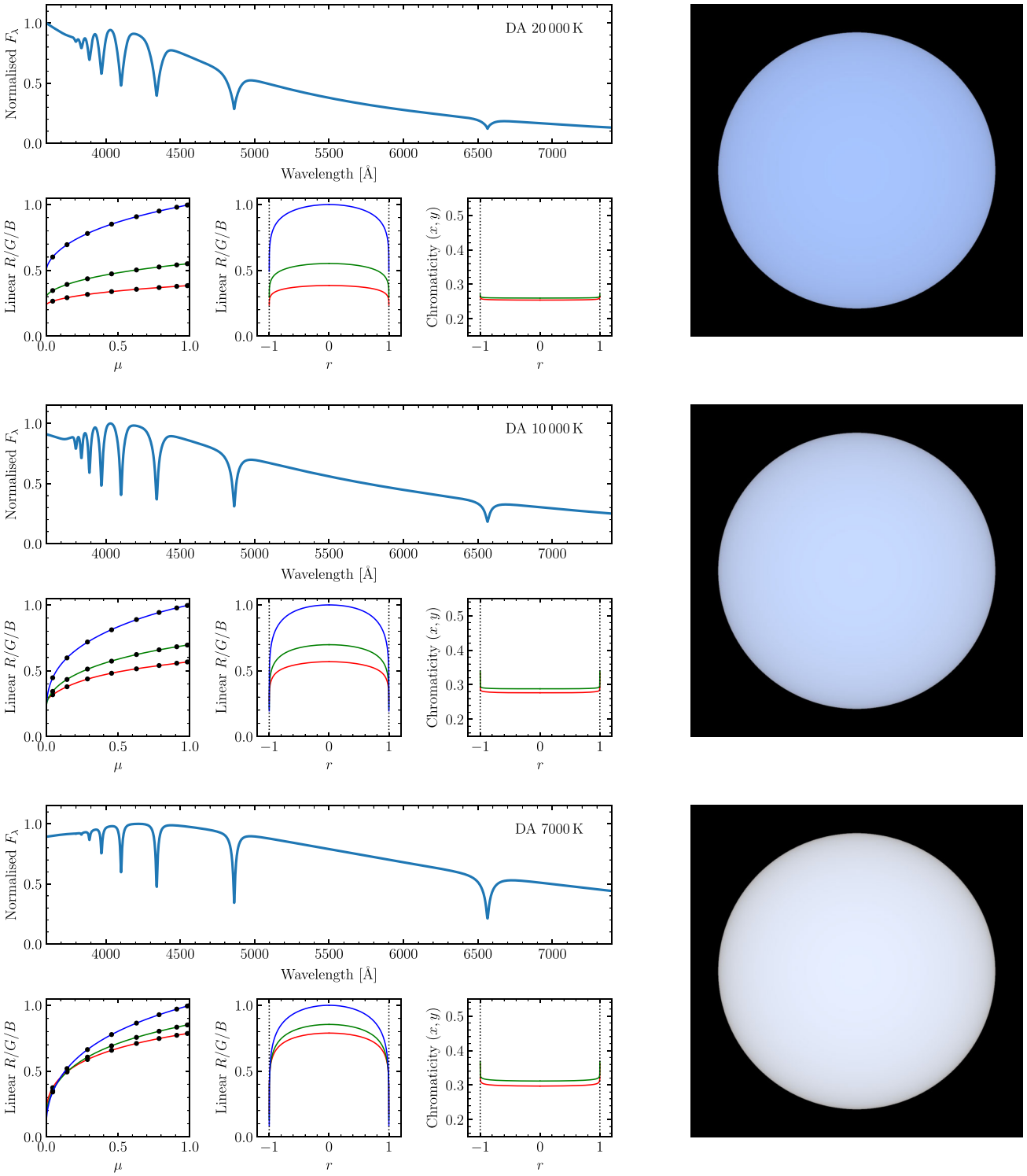

Figure B8. Visualizations for three DA white dwarf models at different $T_{\rm eff}$ (right). The bottom left panels (per object) show the relative intensities in the sRGB channels (red, green, and blue curves respectively) as a function of μ, with Claret 4-parameter curves fitted to the values from the model atmospheres (black dots). The bottom middle panels show the same the same linear intensities as a function of the projected radius, r. The bottom right panels instead show the chromaticity as a function of r, with red and green curves corresponding to x and y values respectively. The top left panels show the disc-averaged spectra used to generate the images.

Downloaded from academic.oup.com/rasti/article/doi/10.1093/rasti/rzag069/8914458 by guest on 26 October 2026

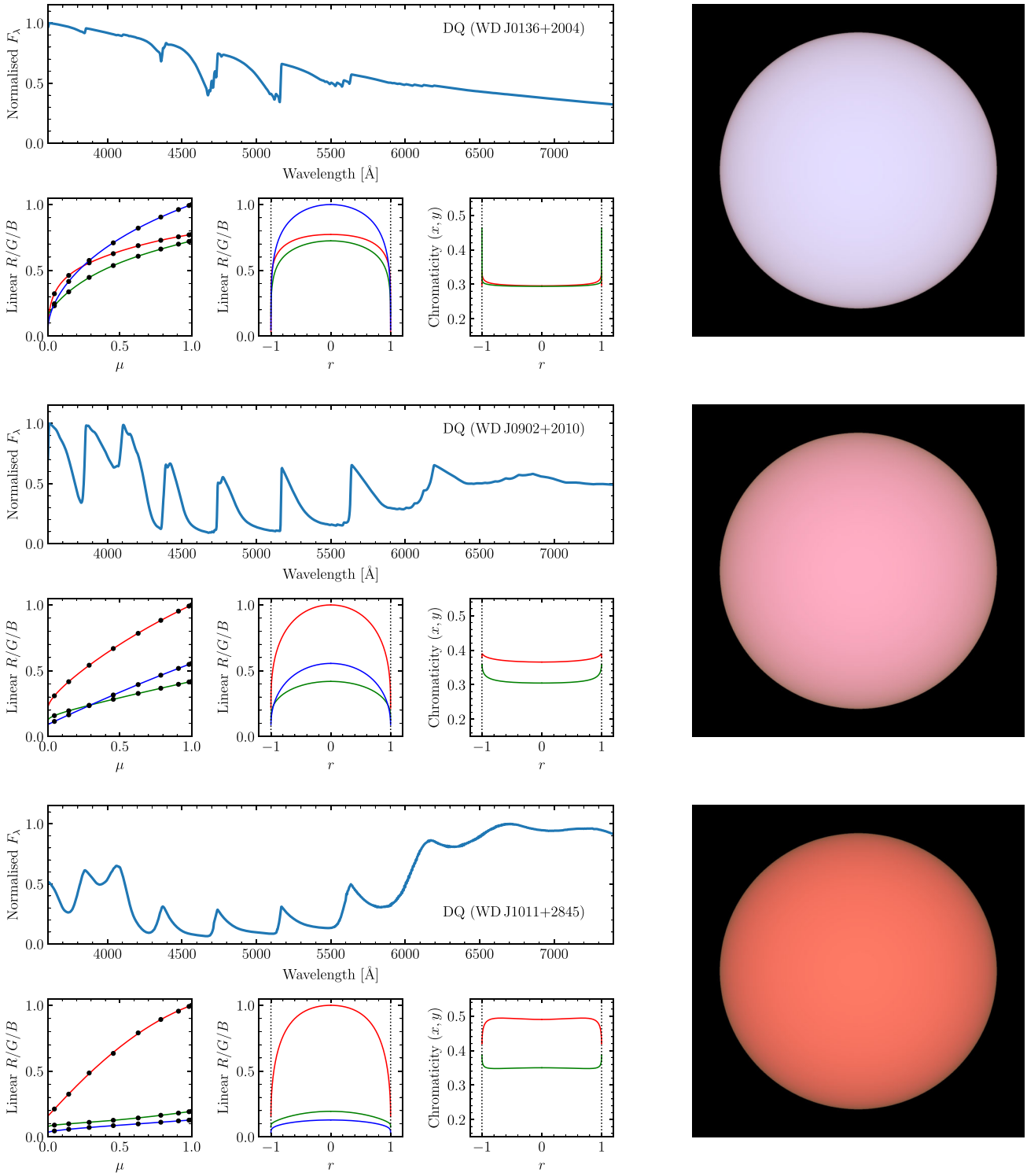

Figure B9. Visualizations for three DQ white dwarf models. Panels to the left of the main images have the same meaning as in Fig. B8.

Downloaded from academic.oup.com/rasti/article/doi/10.1093/rasti/rzag069/8914458 by guest on 26 October 2026

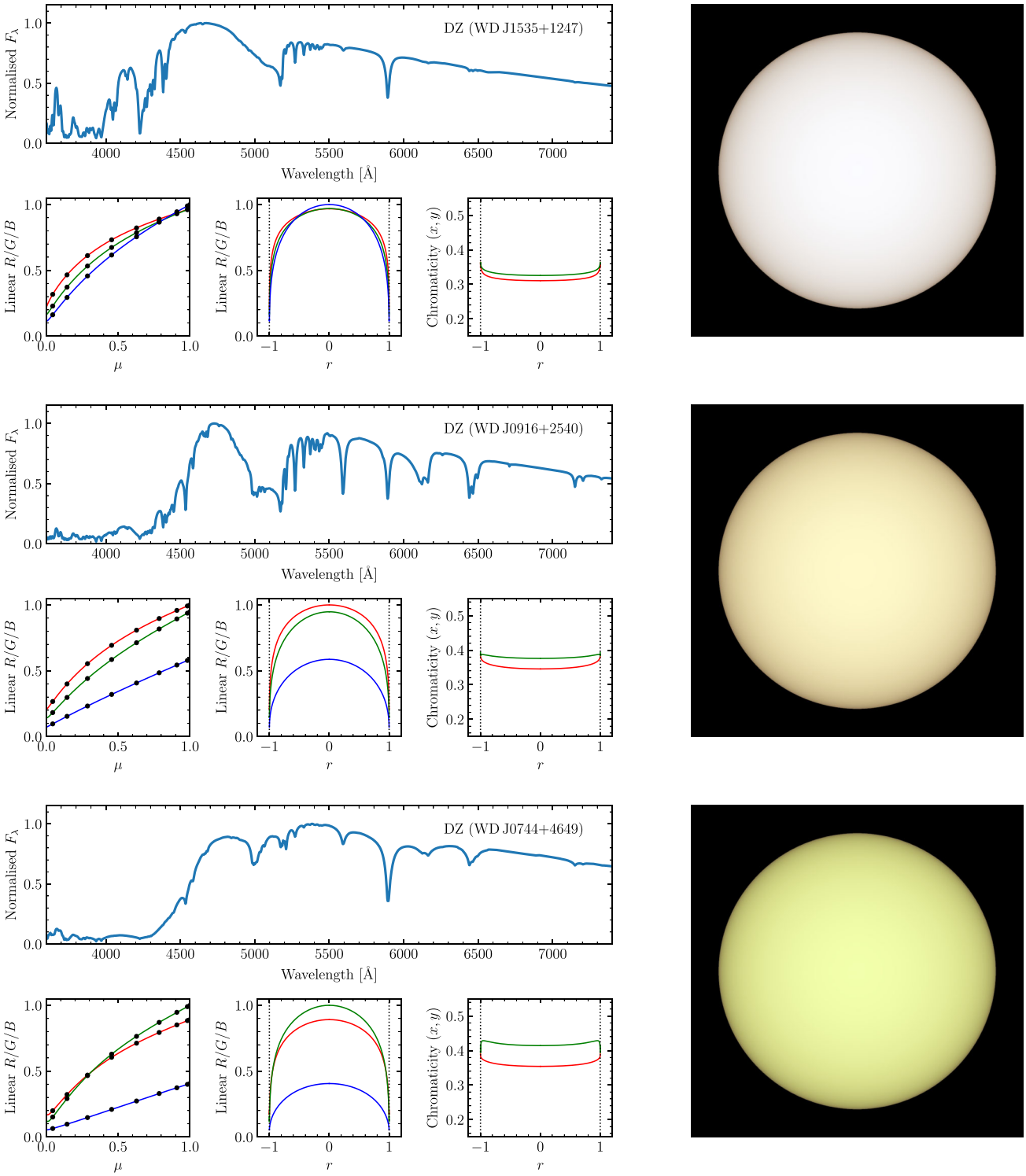

Figure B10. Visualizations for three DZ white dwarf models. Panels to the left of the main images have the same meaning as in Fig. B8.

Downloaded from academic.oup.com/rasti/article/doi/10.1093/rasti/rzag069/8914458 by guest on 26 October 2026

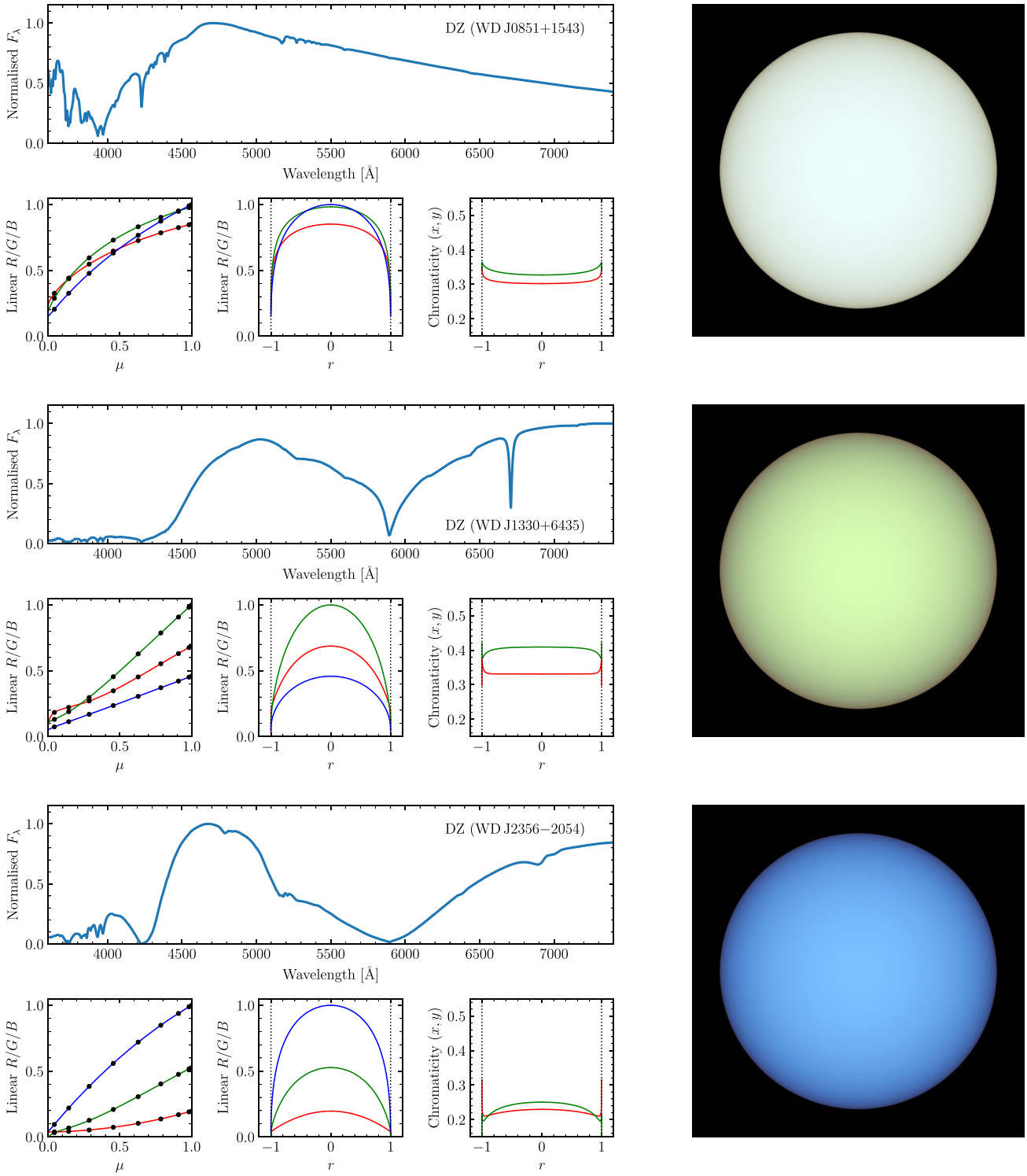

Figure B11. Visualizations for three DZ white dwarf models. Panels to the left of the main images have the same meaning as in Fig. B8.

Downloaded from academic.oup.com/rasti/article/doi/10.1093/rasti/rzag069/8914458 by guest on 26 October 2026

APPENDIX C: ADDITIONAL TABLES

Table C1. Colour information for pure hydrogen (DA) models. (x, y) is the chromaticity and CCT is the correlated colour temperature.

$T_{\rm eff}$ (K)	(x, y)	CCT (K)	Hexcode	$T_{\rm eff}$ (K)	(x, y)	CCT (K)	Hexcode
140 000	(0.242, 0.238)	102 163	#98B3FF	13 500	(0.266, 0.277)	13 046	#B6D1FF
130 000	(0.243, 0.238)	97 064	#98B4FF	13 000	(0.267, 0.279)	12 605	#B8D2FF
120 000	(0.243, 0.238)	91 918	#98B4FF	12 500	(0.268, 0.281)	12 226	#BAD4FF
110 000	(0.243, 0.239)	86 694	#98B4FF	12 000	(0.270, 0.282)	11 837	#BCD5FF
100 000	(0.243, 0.239)	81 394	#98B4FF	11 500	(0.272, 0.284)	11 428	#BFD6FF
90 000	(0.243, 0.240)	76 020	#99B5FF	11 000	(0.274, 0.286)	11 029	#C2D8FF
85 000	(0.243, 0.240)	73 230	#99B5FF	10 500	(0.276, 0.287)	10 633	#C5D9FF
80 000	(0.244, 0.240)	70 387	#99B5FF	10 000	(0.278, 0.289)	10 236	#C9DAFF
75 000	(0.244, 0.240)	67 487	#99B5FF	9500	(0.280, 0.291)	9844	#CCDCFF
70 000	(0.244, 0.241)	64 513	#9AB5FF	9000	(0.283, 0.294)	9441	#D0DEFF
65 000	(0.244, 0.241)	61 440	#9AB6FF	8500	(0.286, 0.296)	9018	#D5E0FF
60 000	(0.244, 0.241)	58 248	#9AB6FF	8000	(0.290, 0.300)	8569	#DBE3FF
55 000	(0.245, 0.242)	54 895	#9AB6FF	7500	(0.294, 0.304)	8087	#E1E7FF
50 000	(0.245, 0.243)	51 324	#9BB7FF	7000	(0.300, 0.310)	7562	#EAECFF
45 000	(0.245, 0.243)	47 433	#9BB7FF	6500	(0.307, 0.317)	6978	#F5F2FF
40 000	(0.246, 0.244)	43 041	#9CB8FF	6000	(0.316, 0.326)	6326	#FFF7FA
35 000	(0.247, 0.246)	37 806	#9DB9FF	5500	(0.331, 0.342)	5571	#FFF0E3
30 000	(0.249, 0.250)	30 368	#9FBCFF	5250	(0.342, 0.353)	5143	#FFEBD4
25 000	(0.252, 0.255)	23 921	#A3C0FF	5000	(0.354, 0.364)	4746	#FFE6C3
20 000	(0.256, 0.261)	19 009	#A8C5FF	4750	(0.366, 0.374)	4406	#FFE0B4
17 000	(0.259, 0.267)	16 356	#ADC9FF	4500	(0.378, 0.384)	4110	#FFDAA5
16 500	(0.260, 0.268)	15 904	#AECAFF	4250	(0.390, 0.392)	3855	#FFD497
16 000	(0.260, 0.269)	15 440	#AFCBFF	4000	(0.402, 0.399)	3643	#FFCF8B
15 500	(0.261, 0.271)	14 971	#B0CCFF	3750	(0.412, 0.404)	3470	#FFCA80
15 000	(0.262, 0.272)	14 494	#B1CDFF	3500	(0.421, 0.409)	3326	#FFC677
14 500	(0.263, 0.274)	14 010	#B3CEFF	3250	(0.429, 0.413)	3209	#FFC26F
14 000	(0.264, 0.275)	13 524	#B4D0FF	3000	(0.435, 0.416)	3120	#FFBF68

Table C2. Colour information for pure helium (DB) models.

$T_{\rm eff}$ (K)	(x, y)	CCT (K)	Hexcode	$T_{\rm eff}$ (K)	(x, y)	CCT (K)	Hexcode
40 000	(0.247, 0.248)	33 532	#9DBBFF	15 000	(0.261, 0.266)	15 803	#B1C8FF
39 000	(0.248, 0.249)	32 372	#9EBCFF	14 000	(0.263, 0.268)	15 004	#B3C9FF
38 000	(0.248, 0.249)	31 287	#9EBCFF	13 000	(0.265, 0.271)	14 050	#B7CBFF
37 000	(0.248, 0.250)	30 258	#9FBCFF	12 000	(0.268, 0.274)	12 996	#BBCEFF
36 000	(0.249, 0.251)	29 276	#9FBDFF	11 000	(0.272, 0.278)	11 882	#C0D1FF
35 000	(0.249, 0.251)	28 332	#A0BDFF	10 000	(0.277, 0.284)	10 755	#C7D6FF
34 000	(0.249, 0.252)	27 419	#A0BEFF	9500	(0.280, 0.287)	10 200	#CBD8FF
33 000	(0.250, 0.253)	26 520	#A1BEFF	9000	(0.283, 0.291)	9662	#D0DBFF
32 000	(0.250, 0.253)	25 645	#A1BFFF	8500	(0.286, 0.294)	9144	#D5DEFF
31 000	(0.251, 0.254)	24 782	#A2C0FF	8000	(0.290, 0.299)	8638	#DAE2FF
30 000	(0.251, 0.255)	23 930	#A2C0FF	7500	(0.294, 0.303)	8125	#E1E6FF
29 000	(0.252, 0.256)	23 089	#A3C1FF	7000	(0.299, 0.309)	7591	#E9EBFF
28 000	(0.252, 0.257)	22 272	#A4C2FF	6500	(0.306, 0.316)	7032	#F4F2FF
27 000	(0.253, 0.258)	21 505	#A4C2FF	6000	(0.314, 0.325)	6438	#FFF8FD
26 000	(0.253, 0.259)	20 834	#A5C3FF	5500	(0.326, 0.336)	5791	#FFF1EA
25 000	(0.254, 0.260)	20 310	#A6C4FF	5250	(0.334, 0.343)	5438	#FFEDDF
24 000	(0.254, 0.260)	19 939	#A6C4FF	5000	(0.344, 0.352)	5061	#FFE8D1
23 000	(0.254, 0.261)	19 648	#A7C4FF	4750	(0.356, 0.362)	4667	#FFE2C2
22 000	(0.255, 0.261)	19 299	#A7C5FF	4500	(0.370, 0.373)	4266	#FFDBB0
21 000	(0.255, 0.262)	18 794	#A8C5FF	4250	(0.387, 0.384)	3875	#FFD29D
20 000	(0.256, 0.263)	18 244	#A9C6FF	4000	(0.406, 0.395)	3512	#FFC989
19 000	(0.257, 0.264)	17 732	#AAC6FF	3750	(0.426, 0.403)	3186	#FFBF76
18 000	(0.258, 0.264)	17 280	#ACC7FF	3500	(0.448, 0.410)	2874	#FFB462
17 000	(0.259, 0.265)	16 867	#ADC7FF	3250	(0.472, 0.415)	2569	#FFA84C
16 000	(0.260, 0.265)	16 409	#AFC7FF	3000	(0.492, 0.417)	2353	#FF9E3B

Downloaded from academic.oup.com/rasti/article/doi/10.1093/rasti/rzag069/8914458 by guest on 26 October 2026

Table C3. Colour information for IR-faint white dwarf spectra.

WD J	(x, y)	CCT (K)	Hexcode	WD J	(x, y)	CCT (K)	Hexcode
003908.38+303539.76	(0.281, 0.320)	8626	#CBF6FF	144440.02+631924.43	(0.295, 0.318)	7753	#E1F4FF
085443.36+350353.26	(0.387, 0.400)	3985	#FFDD96	170320.13+271106.89	(0.336, 0.355)	5380	#FFF5DB
094722.99+445948.59	(0.338, 0.347)	5281	#FFEBD9	172748.75+080819.54	(0.353, 0.362)	4743	#FFE4C4
100103.50+390341.05	(0.321, 0.348)	6001	#FAFFEC	223954.13+001847.11	(0.331, 0.339)	5570	#FFEDE3
125106.16+440303.04	(0.262, 0.286)	12 738	#AED9FF	225817.72+012811.62	(0.304, 0.330)	6969	#F0FFFE
133739.41+000142.66	(0.321, 0.342)	6003	#FFFEF0	231130.15+283444.82	(0.300, 0.334)	7154	#E6FFFA
140237.32+080519.16	(0.287, 0.317)	8282	#D5F4FF	234931.17−080245.64	(0.302, 0.322)	7211	#EDF8FF
140324.75+453333.02	(0.278, 0.318)	8920	#C5F5FF				

Table C4. Colour information for DQ spectra.

WD J	(x, y)	CCT (K)	Hexcode	WD J	(x, y)	CCT (K)	Hexcode
013655.67+200429.88	(0.295, 0.281)	8781	#E3D1FF	114136.50+383611.86	(0.358, 0.303)	4109	#FFB2CC
014519.42+231753.94	(0.286, 0.288)	9450	#D5D8FF	115933.13+130031.54	(0.316, 0.289)	6654	#FFD4FD
032054.12−071625.45	(0.320, 0.293)	6319	#FFD2F7	120154.71+340055.34	(0.325, 0.318)	5900	#FFE3EE
074008.46+181047.41	(0.296, 0.300)	8067	#E4E2FF	123313.51+082402.65	(0.310, 0.312)	6839	#F9EEFF
080558.85+072449.19	(0.341, 0.338)	5111	#FFE0D7	123752.23+415624.69	(0.338, 0.294)	5135	#FFBFE2
080843.15+464028.64	(0.377, 0.327)	3649	#FFB4B6	124739.13+064604.30	(0.407, 0.376)	3335	#FFBC90
082005.03+520453.60	(0.317, 0.295)	6532	#FFD8FB	130945.66+444541.02	(0.296, 0.292)	8275	#E5DBFF
083231.55−040806.97	(0.323, 0.284)	6200	#FFC7F4	131147.07+292349.67	(0.366, 0.303)	3762	#FFACC4
085239.66+042804.48	(0.274, 0.270)	12 517	#C4CAFF	133359.84+001655.03	(0.387, 0.306)	3063	#FF9DB3
085626.95+451337.01	(0.275, 0.262)	13 386	#C6C3FF	135516.62+363612.70	(0.285, 0.284)	9775	#D4D5FF
085914.71+325712.16	(0.278, 0.275)	11 251	#CBCDFF	135628.24−000941.34	(0.311, 0.302)	6911	#FAE3FF
085935.89+601616.14	(0.287, 0.296)	9002	#D6E0FF	145725.28+210747.81	(0.322, 0.319)	6026	#FFE7F1
090208.37+201051.57	(0.384, 0.320)	3346	#FFA9B2	150126.78+210056.68	(0.329, 0.314)	5674	#FFDAE9
093537.00+002422.00	(0.371, 0.316)	3742	#FFB1BE	155413.52+033634.74	(0.304, 0.313)	7224	#F0EFFF
095051.75+122758.93	(0.427, 0.389)	3054	#FFB67B	161414.19+172901.23	(0.355, 0.334)	4541	#FFCEC9
101141.58+284559.07	(0.463, 0.347)	2147	#FF8775	180302.55+232044.14	(0.416, 0.374)	3127	#FFB58A
102801.78+351258.64	(0.360, 0.333)	4332	#FFC8C4	183500.11+642917.66	(0.316, 0.286)	6688	#FFD1FD
111341.34+014642.06	(0.360, 0.315)	4160	#FFBAC8	231030.26−005745.76	(0.294, 0.289)	8610	#E1D9FF

Table C5. Colour information for DZ models.

WD J	(x, y)	CCT (K)	Hexcode	WD J	(x, y)	CCT (K)	Hexcode
004757.08+162836.45	(0.308, 0.321)	6830	#F7F7FF	115748.35+613845.96	(0.295, 0.305)	7991	#E3E7FF
015848.99−094225.19	(0.309, 0.326)	6760	#F8FCFF	115809.40+184557.49	(0.291, 0.292)	8705	#DDDCFF
025206.01−040130.28	(0.290, 0.300)	8531	#DBE3FF	132144.04−023751.47	(0.322, 0.349)	5949	#FBFFEA
073635.21+411828.68	(0.369, 0.394)	4430	#FFEBAB	133001.17+643523.69	(0.332, 0.404)	5531	#DDFFB8
074414.64+464912.63	(0.361, 0.421)	4744	#F6FFA3	133059.42+302953.65	(0.313, 0.328)	6492	#FFFEFF
080626.70+305555.81	(0.300, 0.322)	7291	#EBF8FF	135123.88+264546.53	(0.331, 0.374)	5552	#F3FFD2
080740.69+493059.73	(0.365, 0.391)	4523	#FFEDB0	143007.16−015129.66	(0.320, 0.338)	6086	#FFFDF3
085100.24+154302.04	(0.308, 0.336)	6712	#F1FFF8	150028.03+231554.04	(0.300, 0.310)	7508	#EBECFF
085217.60+340211.27	(0.325, 0.352)	5804	#FDFFE7	153505.81+124745.20	(0.317, 0.332)	6237	#FFFAF7
090146.88+075206.86	(0.302, 0.316)	7298	#EDF2FF	154022.80+535239.89	(0.298, 0.309)	7664	#E8EBFF
090244.75+100459.69	(0.292, 0.309)	8144	#DDEBFF	154201.78+465020.25	(0.315, 0.329)	6378	#FFFCFB
091621.31+254029.10	(0.353, 0.381)	4817	#FFF3BF	154510.32+523618.18	(0.313, 0.334)	6446	#FBFFFA
095645.15+591240.64	(0.278, 0.283)	10 605	#CAD5FF	163601.35+161907.51	(0.387, 0.420)	4109	#FFE98E
102438.07+101410.60	(0.321, 0.335)	6065	#FFF8F2	164939.23+223807.22	(0.335, 0.343)	5393	#FFEBDE
103809.19−003622.45	(0.287, 0.304)	8673	#D6E8FF	182458.45+121316.82	(0.380, 0.395)	4131	#FFE09F
104658.11+132911.33	(0.337, 0.361)	5342	#FFF8D8	222503.65+233855.87	(0.290, 0.301)	8496	#DBE4FF
105533.75+372543.21	(0.347, 0.393)	5053	#F9FFBF	223507.66−005607.73	(0.303, 0.320)	7147	#EFF6FF
113209.59+332353.03	(0.309, 0.321)	6776	#F9F6FF	235645.10−205449.94	(0.222, 0.234)	-	#70B4FF

Downloaded from academic.oup.com/rasti/article/doi/10.1093/rasti/rzag069/8914458 by guest on 26 October 2026

Table C6. Colour information for white dwarfs within 20 pc of the Sun. Surface gravities are in cgs units.

WD J	Alt. name	SpT	$T_{\rm eff}$ (K)	log *g* (dex)	(x, y)	CCT (K)	Hexcode	ref	note
000210.72−430955.39	GJ 915	DA	8428	8.354	(0.287, 0.297)	8926	#D6E1FF	1	
000240.09−341339.59	LHS 1008	DC	6332	8.143	(0.309, 0.319)	6826	#F8F4FF	1	
000720.55+123021.16	LP 464−57	DCP	5223	8.274	(0.345, 0.356)	5027	#FFEACF	1	
001214.75+502520.74	LHS 1038	DA	6483	8.237	(0.307, 0.317)	6933	#F6F3FF	1	
001349.89−714954.26	L 50−73	DAH	6275	7.874	(0.311, 0.321)	6677	#FCF7FF	1	
001412.79−131101.09	G 158−45	DAH	5871	8.212	(0.321, 0.331)	6066	#FFF5F2	1	
004126.03−222102.29	LHS 1126	DQ	5368	7.990	(0.329, 0.344)	5658	#FFF4E5	2	
004909.90+052318.99	van Maanen 2	DZA	5830	8.09	(0.305, 0.320)	7067	#F2F5FF	3	
011800.08+161020.56	LHS 1227	DQ	9278	8.078	(0.281, 0.289)	9957	#CDD9FF	1	a
012403.99−424038.43	LP 991−16	DAH	6080	7.583	(0.314, 0.324)	6466	#FFF8FD	1	
012524.47−260044.45	GJ 1039	DC	6941	8.227	(0.300, 0.310)	7527	#EAECFF	1	
013759.39−045944.67	L 870−2	DA+DA	7454	7.906	(0.295, 0.305)	8039	#E2E7FF	3	b
			7162	7.809	(0.298, 0.308)	7730	#E7EAFF		
014300.98−671830.35	L 88−59	DAZ	6350	7.981	(0.310, 0.320)	6768	#F9F5FF	1	
015151.14+642552.55	GJ 3118	DA	8794	8.098	(0.285, 0.295)	9247	#D3DFFF	1	
015202.96+470006.66	GD 279	DA	14 293	7.999	(0.264, 0.274)	13 810	#B3CFFF	1	
021026.11−504926.33	GJ 86B	DC	8180	8.020	(0.288, 0.297)	8812	#D8E1FF	4	c
021120.84+395521.52	LHS 151	DAZ	7196	7.933	(0.298, 0.307)	7760	#E6EAFF	1	
021228.98−080411.00	LP 649−67	DA	8467	7.893	(0.287, 0.297)	9000	#D5E0FF	1	
021348.83−334530.03	LP 941−19	DAZ	5618	8.020	(0.327, 0.338)	5725	#FFF1E8	5	
023237.91−141151.77	LHS 1415	DA	5393	7.986	(0.335, 0.346)	5381	#FFEEDD	1	
023521.79−240047.12	LP 830−14	DAH	4871	7.529	(0.357, 0.366)	4645	#FFE4BF	1	
024836.43+542322.46	LHS 1446	DAZ	4942	8.018	(0.356, 0.367)	4659	#FFE5C0	1	
031031.02−683603.38	LB 3303	DA	15 866	8.077	(0.261, 0.270)	15 107	#AFCCFF	1	
032511.05−014915.05	LHS 1547	DAZH	5165	8.048	(0.346, 0.357)	4988	#FFE9CE	1	
034434.85+182609.82	GJ 151	DQ	6837	8.097	(0.303, 0.308)	7374	#EEE9FF	6	
040026.68+081406.93	GJ 3259	DA	5461	7.934	(0.332, 0.343)	5514	#FFEFE1	1	
041521.80−073929.20	40 Eridani B	DA	16 265	7.916	(0.260, 0.268)	15 880	#AECAFF	1	
041630.04−591757.19	ϵ Reticuli B	DA	14 271	7.824	(0.263, 0.273)	14 177	#B2CEFF	1	
042553.73+121148.34	LP 475−70	DC	6153	8.213	(0.312, 0.322)	6621	#FDF7FF	1	
043112.57+585841.29	Stein 2051 B	DC	7011	8.098	(0.299, 0.309)	7604	#E9EBFF	1	
043644.90+270951.52	G 39−27	DA	5534	8.023	(0.330, 0.341)	5610	#FFF0E4	1	
043747.41−084910.62	LHS 194	DQ	6601	8.050	(0.308, 0.310)	6984	#F6ECFF	6	
050552.46−172243.48	GJ 3329	DAH	5345	7.864	(0.337, 0.347)	5330	#FFEDDB	1	
053344.80+015643.45	GJ 207.1 B	-	6100	8.0	(0.314, 0.325)	6445	#FFF8FD	7	d
055119.48−001021.11	G 99−37	DQ	6053	8.122	(0.323, 0.330)	5967	#FFF1F0	6	
055443.04−103521.34	WD 0552−106	DZ	6578	8.177	(0.305, 0.315)	7120	#F2F1FF	1	
055509.53−041007.07	LP 658−2	DZ	4642	8.098	(0.362, 0.378)	4531	#FFE6B6	3	
055625.46+052148.44	G 99−47	DAH	5729	8.151	(0.325, 0.336)	5852	#FFF3EC	1	
060529.40+604922.46	LHS 1817 B	-	6300	8.0	(0.311, 0.321)	6699	#FBF6FF	7	d
064509.30−164300.72	Sirius B	DA	25 970	8.570	(0.252, 0.256)	22 628	#A4C1FF	8	
064722.15+023108.91	GJ 3410	DA	7109	8.594	(0.299, 0.309)	7650	#E8EBFF	1	
064737.99+373057.06	LAWD 23	DA	21 394	8.145	(0.255, 0.260)	19 627	#A7C4FF	1	
065705.91−390935.68	L 454−9	DA	6370	8.080	(0.309, 0.319)	6785	#F9F5FF	1	
070051.66+315743.83	LHS 1889	DA	4873	7.907	(0.359, 0.369)	4582	#FFE3BC	1	
070852.28−670631.43	WD 0708−670	DCP	4862	7.860	(0.359, 0.369)	4574	#FFE3BC	1	
073046.96+481006.27	G 107−70 B	DA	4926	8.100	(0.358, 0.368)	4623	#FFE4BE	2	c
073046.99+481005.67	G 107−70 A	DA	4934	7.890	(0.356, 0.366)	4671	#FFE5C0	2	c
073330.88+640927.44	GJ 1098	DA	5140	7.824	(0.346, 0.356)	5000	#FFE9CE	1	
073917.88+051326.80	Procyon B	DQZ	7585	7.960	(0.289, 0.296)	8799	#D9E0FF	2	c
074020.79−172449.16	LAWD 25	DZA	7450	7.972	(0.289, 0.297)	8756	#D9E1FF	3	
074538.43−335551.34	GJ 288 B	DC	4293	7.798	(0.388, 0.390)	3911	#FFD69A	1	
075014.58+071148.92	GJ 1102 B	DC	4280	7.783	(0.388, 0.390)	3899	#FFD59A	1	
075015.34+071137.10	GJ 1102 A	DC	4680	7.894	(0.369, 0.376)	4332	#FFDFB0	1	
075308.14−674731.38	L 97−12	DA	5630	7.948	(0.327, 0.337)	5757	#FFF2E9	1	
075356.62−252401.48	WD 0751−252	DA	4939	7.897	(0.356, 0.366)	4677	#FFE5C0	1	
080653.75−661816.70	L 97−3	DQ	10 393	8.041	(0.275, 0.282)	11 165	#C5D4FF	1	a
081227.07−352943.32	WD 0810−353	DAH	6239	8.178	(0.312, 0.322)	6597	#FDF8FF	1	

Downloaded from academic.oup.com/rasti/article/doi/10.1093/rasti/rzag069/8914458 by guest on 26 October 2026

Table C6 – *continued*

WD J	Alt. name	SpT	$T_{\rm eff}$ (K)	log g (dex)	(x, y)	CCT (K)	Hexcode	ref	note
081411.17+484529.81	G 111−64	DC	6709	8.119	(0.303, 0.313)	7257	#EFEFFF	1	
081840.26−311020.33	WD 0816−310	DZ	6754	8.263	(0.295, 0.311)	7829	#E3EEFF	9	
082126.70−670320.02	WD 0820−668	DA	4793	7.902	(0.363, 0.372)	4475	#FFE1B7	1	
084132.43−325632.92	GJ 318	DA	9086	7.770	(0.282, 0.293)	9563	#CFDDFF	1	
084248.46−134713.21	LP 726−1	DZ	5388	8.174	(0.335, 0.365)	5424	#FFFFDA	9	
085912.92−005842.86	LP 606−32	DC	4997	7.947	(0.353, 0.364)	4753	#FFE6C4	1	
091556.08+532523.86	G 195−19	DCP	7155	8.217	(0.298, 0.307)	7757	#E6E9FF	1	
100149.36+144123.79	G 42−33	DC	6778	8.206	(0.302, 0.312)	7338	#EEEEFF	1	
101141.58+284559.07	LHS 2229	DQpec	4335	8.211	(0.463, 0.347)	2151	#FF8775	10	e
101201.87−184333.27	WD 1009−184	DZ	6394	8.183	(0.305, 0.319)	7048	#F2F4FF	9	
102309.06+632741.49	LP 62−147	DA	6801	8.033	(0.303, 0.312)	7313	#EEEEFF	1	
103702.48+711058.70	LHS 285	DC	4693	8.155	(0.369, 0.377)	4314	#FFDEAF	1	
103855.57−204056.83	LHS 2293	DQ	5754	8.557	(0.358, 0.302)	4092	#FFB1CC	2	
104539.04−190645.03	GJ 401 B	DQ	5736	7.875	(0.325, 0.324)	5869	#FFE8ED	6	
105735.13−073123.18	LHS 2333	DC	7096	8.245	(0.298, 0.308)	7696	#E7EAFF	1	
111827.20−472156.96	WD 1116−470	DC	5910	8.077	(0.316, 0.327)	6316	#FFF7F9	1	
112412.97+212135.57	Ross 627	DA	7373	8.037	(0.296, 0.305)	7944	#E3E8FF	1	
113430.48−325002.40	GJ 432 B	DZ	5178	8.024	(0.333, 0.342)	5481	#FFEEE0	3	
113705.10+294758.29	GD 140	DA	21 336	8.517	(0.256, 0.263)	18 415	#A9C6FF	1	
114542.92−645029.46	LAWD 37	DQ	8062	8.058	(0.284, 0.289)	9629	#D1DAFF	6	
114734.45−745759.24	WD 1145−747	DC	3821	7.742	(0.409, 0.403)	3524	#FFCC84	1	
115052.33+683115.97	WD 1148+687	DA	6696	8.258	(0.304, 0.314)	7177	#F1F0FF	1	
120526.67−233312.14	LP 852−7	DAZ	8540	7.959	(0.286, 0.296)	9055	#D5E0FF	1	
121129.27+572417.24	G 197−47	DAZ	5829	7.982	(0.321, 0.332)	6044	#FFF4F2	1	
122642.02−661218.47	GJ 2092	DA	7582	7.897	(0.294, 0.303)	8166	#E0E6FF	1	
123849.78−494800.22	GJ 2095	DA	11 359	8.688	(0.274, 0.287)	10 813	#C3D9FF	1	
130009.06+032841.06	GJ 492	DA	5650	8.190	(0.327, 0.339)	5724	#FFF2E8	1	
130841.20+850228.16	G 256−7	DAH	5254	8.077	(0.342, 0.353)	5128	#FFEBD3	1	
131256.47−472807.91	GJ 3770	DC	3855	7.695	(0.407, 0.402)	3549	#FFCC85	1	
131924.74−214754.87	LP 854−50	DA	5882	8.618	(0.322, 0.333)	5998	#FFF5F0	1	
131925.56−782328.17	LAWD 45	DAH	5542	8.129	(0.330, 0.342)	5590	#FFF0E4	1	
133013.64−083429.47	GJ 515	DA	14 563	7.971	(0.263, 0.273)	14 139	#B2CEFF	1	
133631.85+034045.94	Wolf 489	DA	4858	7.821	(0.359, 0.369)	4575	#FFE3BC	1	
134121.80+050045.85	WD 1338+052	DC	4022	7.746	(0.400, 0.398)	3671	#FFD08D	1	
134803.01+233446.44	LP 380−5	DC	4576	7.767	(0.373, 0.380)	4222	#FFDCAB	1	
135315.53−091633.37	GJ 3814	DAH	8881	8.325	(0.284, 0.295)	9295	#D2DFFF	1	
141159.17−592044.99	WD 1408−591	DA	6653	8.108	(0.305, 0.315)	7137	#F1F0FF	1	
144725.34−174215.75	LHS 378	DC	4980	8.448	(0.357, 0.368)	4639	#FFE4BE	1	
153505.81+124745.20	G 137−24	DZ	5790	7.985	(0.317, 0.332)	6237	#FFFAF7	11	
154730.02−375508.46	LAWD 60	DA	10 392	8.026	(0.276, 0.288)	10 525	#C6D9FF	1	
162333.84−391346.16	WD 1620−391	DA	24 073	8.006	(0.252, 0.256)	22 759	#A4C1FF	1	
162825.00+364615.85	Ross 640	DZ	8964	8.224	(0.281, 0.289)	9906	#CEDAFF	12	
163233.17+085122.67	G 138−38	DA	5594	8.016	(0.328, 0.339)	5693	#FFF1E7	1	
163421.55+571008.87	LHS 422	DQ	6126	8.020	(0.313, 0.324)	6516	#FFF9FF	6	
163501.43+431736.35	G 180−63	DAZ	6516	8.153	(0.307, 0.317)	6982	#F5F2FF	1	
164825.63+590322.66	G 226−29	DA	12 182	8.285	(0.270, 0.283)	11 669	#BDD6FF	1	
170641.36−264334.71	WD 1703−267	DAH	6128	8.343	(0.315, 0.325)	6433	#FFF8FC	1	
170807.97+025737.08	GJ 1211	DZ	6720	8.242	(0.298, 0.310)	7691	#E7ECFF	9	
170931.54+434052.77	G 203−47 B	-	5286	8.0	(0.340, 0.351)	5199	#FFECD6	7	d
174736.82−543631.16	WD 1743−545	DC	4358	7.821	(0.384, 0.388)	3975	#FFD79E	1	
174807.99+705235.92	G 240−72	DXP	5137	8.060	(0.338, 0.347)	5274	#FFEBD9	1	
174950.15+824626.06	LHS 56	DA	7188	7.868	(0.298, 0.307)	7754	#E6EAFF	1	
181706.50+132824.99	WD 1814+134	DA	4873	7.803	(0.358, 0.368)	4600	#FFE3BD	1	
182119.83+610107.38	G 227−28	DA	4823	7.765	(0.361, 0.370)	4537	#FFE2BA	1	
182404.55−130842.29	GJ 2135	DAZ	6079	8.022	(0.315, 0.325)	6417	#FFF8FC	1	
182524.24+113557.34	WD 1823+116	DA	4883	7.885	(0.359, 0.368)	4599	#FFE3BD	1	
183020.27+544727.21	G 227−35	DXP	6711	8.473	(0.304, 0.314)	7182	#F1F0FF	1	
190010.25+703951.42	GJ 742	DAH	12 540	8.671	(0.271, 0.284)	11 547	#BDD6FF	1	
191858.63+384321.48	GJ 1234	DZ	5743	7.939	(0.312, 0.322)	6589	#FEF8FF	3	

Downloaded from academic.oup.com/rasti/article/doi/10.1093/rasti/rzag069/8914458 by guest on 26 October 2026

Table C6 – *continued*

WD J	Alt. name	SpT	$T_{\rm eff}$ (K)	log g (dex)	(x, y)	CCT (K)	Hexcode	ref	note
192034.92−074000.07	LAWD 74	DBQA	10 805	8.051	(0.273, 0.279)	11 639	#C2D2FF	1	
192126.76+061322.71	WD1919+061	DA	5908	8.147	(0.319, 0.330)	6142	#FFF5F5	1	
192140.42+144041.40	GD 219	DA	15 162	8.151	(0.263, 0.273)	14 254	#B2CEFF	1	
193713.75+274318.74	GJ 1241	DA	12 022	8.046	(0.270, 0.282)	11 803	#BDD5FF	1	
195629.23−010232.67	LHS 3501	DAH	7790	8.168	(0.292, 0.302)	8353	#DEE5FF	1	
200502.20+542603.23	Wolf 1130 B	-	6100	8.8	(0.314, 0.325)	6445	#FFF8FD	7	d
200534.87−105654.43	LHS 483	DC	4577	8.142	(0.375, 0.381)	4181	#FFDCA9	1	
201056.85−301306.63	GJ 2147	DA	15 124	7.940	(0.262, 0.271)	14 741	#B1CCFF	1	
201231.78−595651.67	WD 2008−600	DC	4905	7.770	(0.351, 0.358)	4822	#FFE5C8	2	
202025.46−302714.65	WD 2017−306	DC	9934	8.045	(0.277, 0.284)	10 677	#C8D6FF	1	
203421.89+250349.75	Wolf 1346	DAZ	20 145	7.932	(0.255, 0.261)	19 311	#A8C4FF	1	
204421.46−680521.36	GJ 2149	DA	16 420	8.463	(0.262, 0.272)	14 610	#B0CDFF	1	
204906.70+372814.05	LP 284−13	DAP	14 710	8.297	(0.264, 0.276)	13 520	#B4D0FF	1	
205020.65+263040.76	G187−8	DA	4909	7.270	(0.353, 0.362)	4756	#FFE5C4	1	
205213.41−250415.13	WD 2049−253	DCP	4908	7.853	(0.357, 0.367)	4640	#FFE4BF	1	
205647.78−045039.54	Ross 193 B	DC	4416	7.879	(0.382, 0.386)	4031	#FFD8A1	1	
210105.20−490624.27	WD 2058−493	DA	5118	7.922	(0.347, 0.358)	4942	#FFE9CC	1	
211316.85−814912.88	LAWD 83	DAZH	9914	8.242	(0.279, 0.290)	10 081	#CADBFF	1	
211856.26+541241.24	G 231−40	DA	14 785	7.899	(0.262, 0.272)	14 511	#B1CDFF	1	
214157.57−330029.80	L570−26	DZ	7113	8.132	(0.291, 0.306)	8318	#DBE9FF	9	
214241.01+205958.12	LHS 3703	DQ	8495	8.090	(0.272, 0.284)	11 343	#C0D6FF	2	
214324.09−065947.99	WD 2140−072	DA	8905	8.424	(0.284, 0.295)	9303	#D2DFFF	1	
215140.11+591734.85	WD 2150+591	DAH	5105	7.987	(0.348, 0.359)	4906	#FFE8CA	1	
215738.36−510031.52	GJ 841 B	DQ	6549	7.969	(0.321, 0.307)	6178	#FFDEF5	6	
220420.86−751326.06	LHS 3752	DA	8875	8.628	(0.284, 0.295)	9264	#D2DFFF	1	
221434.75−385907.27	WD 2211−392	DA	6063	8.353	(0.316, 0.326)	6350	#FFF8FA	1	
223033.53−751524.30	WD 2226−755	DC	3911	7.727	(0.405, 0.400)	3588	#FFCD88	1	
223039.98−751355.24	WD 2226−754	DC	4194	7.729	(0.392, 0.393)	3822	#FFD395	1	
224905.55+223631.99	GJ 1273	DA	10 534	8.662	(0.277, 0.289)	10 332	#C7DAFF	1	
225123.02+293944.49	WD 2150+591	DA	5635	7.680	(0.326, 0.336)	5817	#FFF2EB	1	
225353.39−064654.49	LP 701−29	DZ	4041	7.99	(0.408, 0.423)	3685	#FFD87B	3	
230958.53+550649.43	G 233−42 B	DA	5531	8.107	(0.331, 0.342)	5581	#FFF0E3	1	
232847.64+051454.24	G 29−38	DAZ	11 529	8.042	(0.272, 0.284)	11 417	#BFD6FF	1	
233850.74−074119.97	GD 1212	DA	10 873	8.009	(0.274, 0.286)	10 920	#C3D8FF	1	
234350.72+323246.73	G 130−5	DA	12 587	8.004	(0.268, 0.280)	12 293	#BAD3FF	1	

Notes. References: (1) M. W. O'Brien et al. (2024), (2) N. Giammichele et al. (2012), (3) M. W. O'Brien et al. (2026a), (4) J. Farihi et al. (2013), (5) O. Vincent et al. (2024), (6) P. Bergeron et al. (1997), (7) M. W. O'Brien et al. (2026b), (8) P.-E. Tremblay et al. (2017), (9) S. Coutu et al. (2019), (10) S. Blouin & P. Dufour (2019), (11) M. A. Hollands et al. (2022), (12) S. Blouin et al. (2018).
(a) Weak carbon/metal features. Colour calculations were performed with pure helium model grids. (b) Object is an unresolved double-degenerate binary. Parameters for each component are averages from the provided reference. (c) Object is absent from *Gaia* DR3, with parameters adopted from the accompanying reference. (d) White dwarf is part of post-common-envelope binary with atmospheric parameters determined from UV spectroscopy, and a DA spectral type assumed for colour calculations. (e) Spectrum was obtained from the SDSS.

This paper has been typeset from a TEX/LATEX file prepared by the author.

© The Author(s) 2026. Published by Oxford University Press on behalf of Royal Astronomical Society. This is an Open Access article distributed under the terms of the Creative Commons Attribution License (https://creativecommons.org/licenses/by/4.0/), which permits unrestricted reuse, distribution, and reproduction in any medium, provided the original work is properly cited.

Downloaded from academic.oup.com/rasti/article/doi/10.1093/rasti/rzag069/8914458 by guest on 26 October 2026